1

OFFICE OF NAVAL RESEARCH

CONTRACT NO. N0014-89-J-1746

R & T CODE 413r001

TECHNICAL REPORT NO. 3

Experimental and Theoretical Study of Inhomogeneous Electron Transfer in Betaine: Comparisons of Measured and Predicted Spectral Dynamics

Alan E. Johnson, Nancy E. Levinger, Wlodzimierz Jarzeba, Ralph E. Schlief, Dahv A. V. Kliner, and Paul F. Barbara

Chemical Physics, in press

University of Minnesota
Department of Chemistry
Minneapolis, MN 55455

May 15, 1993

63pg

Unclassified
SECURITY CLASSIFICATION OF THIS PAGE

REPORT DOCUMENTATION PAGE

Form Approved
OMB No. 0704-0188

1a REPORT SECURITY CLASSIFICATION: Unclassified

1b RESTRICTIVE MARKINGS

2a SECURITY CLASSIFICATION AUTHORITY

2b DECLASSIFICATION / DOWNGRADING SCHEDULE

3 DISTRIBUTION / AVAILABILITY OF REPORT: Approved for public release distribution unlimited

4 PERFORMING ORGANIZATION REPORT NUMBER(S): Technical Report No. 3

5 MONITORING ORGANIZATION REPORT NUMBER(S)

6a NAME OF PERFORMING ORGANIZATION: Department of Chemistry University of Minnesota

6b OFFICE SYMBOL (If applicable)

7a NAME OF MONITORING ORGANIZATION: Office of Naval Research

6c ADDRESS (City, State, and ZIP Code)
207 Pleasant St. SE
Minneapolis, MN 55455

7b ADDRESS (City, State, and ZIP Code)
Chemistry Program
800 North Quincy St.
Arlington, VA 22217

8a NAME OF FUNDING / SPONSORING ORGANIZATION: Office of Naval Research

8b OFFICE SYMBOL (If applicable)

9 PROCUREMENT INSTRUMENT IDENTIFICATION NUMBER: N0014-89-J-1746

8c ADDRESS (City, State, and ZIP Code)
Chemistry Program, 800 N. Quincy St.
Arlington, VA 22217

10 SOURCE OF FUNDING NUMBERS

PROGRAM ELEMENT NO.	PROJECT NO.	TASK NO	WORK UNIT ACCESSION NO.

11 TITLE (Include Security Classification): Experimental and Theoretical Study of Inhomogeneous Electron Transfer in Betaine: Comparisons of Measured and Predicted Spectral Dynamics

12 PERSONAL AUTHOR(S): A. E. Johnson, N. E. Levinger, W. Jarzeba, R. Schlief, D. A. V. Kliner and P. Barbar

13a TYPE OF REPORT: Technical

13b TIME COVERED FROM TO

14 DATE OF REPORT (Year, Month, Day): May 15, 1993

15 PAGE COUNT

16 SUPPLEMENTARY NOTATION

17 COSATI CODES

FIELD	GROUP	SUB-GROUP

18 SUBJECT TERMS (Continue on reverse if necessary and identify by block number)

19 ABSTRACT (Continue on reverse if necessary and identify by block number)

See abstract on reverse side

20 DISTRIBUTION / AVAILABILITY OF ABSTRACT
☒ UNCLASSIFIED/UNLIMITED ☐ SAME AS RPT ☐ DTIC USERS

21 ABSTRACT SECURITY CLASSIFICATION: Unclassified

22a NAME OF RESPONSIBLE INDIVIDUAL: Dr. Ronald A. De Marco

22b TELEPHONE (Include Area Code)

22c OFFICE SYMBOL

DD Form 1473, JUN 86

Previous editions are obsolete.

S/N 0102-LF-014-6603

SECURITY CLASSIFICATION OF THIS PAGE
Unclassified

19.

Abstract

New tunable pump and probe data are reported for the S_1-S_0 reverse electron transfer in betaine in solution. the observed dynamics are a dramatic function of probe wavelength due to energy deposition into solute and solvent molecular degrees of freedom from the electron transfer. These data indicate that in nonpolar solvents, this energy is primarily deposited into intramolecular modes, but some is specifically deposited into polar collective motions of the solvent, *i.e.* the solvent coordinate. Modern theories of electron transfer that include diffusive motion along the solvent coordinate as a driving mechanism for electron transfer predict this specific energy deposition into the solvent coordinate. In this paper, we extend a model by Walker et al. to predict the spectral dynamics due to solvent coordinate heating caused by the electron transfer and compare to experimental results. We show that the diffusive electron transfer mechanism creates a displaced distribution along the solvent coordinate that is characterized by an absorption spectrum that is red-shifted from the equilibrium ground-state distribution, in agreement with experimental observations. The model is not in quantitative agreement with experiment, however, because it neglects the contributions of vibrational heating of the intramolecular modes to the spectral dynamics. This type of vibrational heating is evident in the observed dynamics in nonpolar solvents.

Chemical Physics
Electron Transfer
Special Issue
Submitted 3/18/93

Experimental and Theoretical Study of Inhomogeneous Electron Transfer in Betaine: Comparisons of Measured and Predicted Spectral Dynamics

Alan E. Johnson, Nancy E. Levinger,[a] Włodzimierz Jarzęba,[b] Ralph E. Schlief, Dahv A.V. Kliner, and Paul F. Barbara*

Department of Chemistry, University of Minnesota, Minneapolis, MN 55455.

---

*Author to whom correspondence should be addressed.

[a] Present Address: Department of Chemistry, Colorado State University, Fort Collins, CO 80523.

[b] On leave from: Faculty of Chemistry, Jagiellonian University, 3 Ingardena, 30–060 Kraków, Poland.

ABSTRACT

New tunable pump and probe data are reported for the $S_1 \rightarrow S_0$ reverse electron transfer in betaine in solution. The observed dynamics are a dramatic function of probe wavelength due to energy deposition into solute and solvent molecular degrees of freedom from the electron transfer. The data indicate that in nonpolar solvents, this energy is primarily deposited into intramolecular modes. In polar solvents, most of the energy is deposited into intramolecular modes, but some is specifically deposited into polar collective motions of the solvent, *i.e.* the solvent coordinate. Modern theories of electron transfer that include diffusive motion along the solvent coordinate as a driving mechanism for electron transfer predict this specific energy deposition into the solvent coordinate. In this paper, we extend a model by Walker *et al.* to predict the spectral dynamics due to solvent coordinate heating caused by the electron transfer and compare to experimental results. We show that the diffusive electron transfer mechanism creates a displaced distribution along the solvent coordinate that is characterized by an absorption spectrum that is red–shifted from the equilibrium ground–state distribution, in agreement with experimental observations. The model is not in quantitative agreement with experiment, however, because it neglects the contributions of vibrational heating of the intramolecular modes to the spectral dynamics. This type of vibrational heating is evident in the observed dynamics in nonpolar solvents.

I. INTRODUCTION

Fast exothermic processes in solution, including internal conversions from excited states, can deposit large quantities of energy into the solvent and into vibrational modes of the reacting molecule(s).[1–7] This paper is concerned with transient spectral effects caused by energy deposition from fast electron transfer in betaine–30. Following optical preparation of the S_1 state by excitation within the $S_0 \rightarrow S_1$ charge–transfer absorption band, betaine undergoes a rapid, reverse $S_1 \rightarrow S_0$ electron transfer.

Scheme 1

Relaxation along nuclear coordinates in the excited state and subsequent electron transfer yields a nonequilibrium, or "hot" ground–state distribution.

We recently reported observations of red–shifted absorption spectra following the $S_1 \rightarrow S_0$ electron transfer in several compounds[1–5] and assigned these spectra to "hot" ground state configurations of the solute/solvent system. The red edge of an electronic absorption band is particularly sensitive to excess internal energy because of vibrational hot bands. In solution, however, these hot bands are obscured by solvent broadening. In addition to vibrational heating, broadening on the red edge can indicate nonequilibrium displacements of the solvent configuration, especially in cases where the electronic absorption spectrum is strongly coupled to the solvent polarity.[1–5]

In recent treatments of electron transfer, the solvent coordinate (a one–dimensional description of the polar, collective motions of the solvent) is often modeled as a classical degree of freedom. Sumi and Marcus[9] assumed that the electron transfer reaction occurs along vibrational degrees of freedom with a rate that depends on the solvent polarization. In the application of their ideas, they used a classical diffusion equation to describe solvent polarization motion. The vibrational coordinates were modeled as a single, average classical coordinate. Jortner and Bixon proposed a related model.[10] However, they modeled the vibrational degrees of freedom as a single, quantized harmonic oscillator whose frequency, like the frequency in Sumi–Marcus theory, corresponds to an average of the true frequencies coupled to the electron transfer. These models are closely related to various forms of inhomogeneous theories of reaction rates.[11]

One interesting limit of these inhomogeneous polarization models occurs in the small barrier regime: the reaction rate can be limited by fluctuations of the solvent polarization. Fluctuations drive the reaction by allowing the molecule to access values of the solvent polarization that have faster rate constants. A closely related behavior has previously been observed in the excited–state electron transfer of bianthryl.[12] In this case, optical excitation of the molecule corresponds to a local excitation of one of the anthracene moieties. Following excitation to this locally excited (LE) state, electron transfer to the charge transfer (CT) state occurs with a rate equal to the rate of polarization fluctuations of the solvent. Therefore, the rate depends on the dynamical properties of the solvent.[13]

Another example of an electron–transfer rate that can depend on the dynamical properties of the solvent is the $S_1 \rightarrow S_0$ electron transfer in betaine.[1–3] Betaine is particularly interesting because optical excitation directly accesses the CT state (rather than some intermediate LE state), which undergoes subsequent electron transfer to reform the ground state. Therefore, the parameters needed to predict the rate can be obtained independently from optical spectroscopy of the $S_0 \rightarrow S_1$ transition,[1,2,4,5,14–16] allowing for direct comparison between electron–transfer theory and experiment. We previously used parameters estimated from the absorption spectrum to predict electron–transfer rates[1,2] using Sumi–Marcus theory[9] and Jortner–Bixon theory.[10] The predictions from Sumi–Marcus theory were orders of magnitude too slow. The predictions from Jortner–Bixon theory were excellent in rapidly relaxing solvents, when the observed rate was well correlated with the rate of solvation dynamics. However, Jortner–Bixon theory predicted rates that were much too slow in slowly relaxing solvents, demonstrating the importance of low–frequency intramolecular fluctuations in driving the electron transfer.

We developed a third model[2] that incorporates the strong points of both the Sumi–Marcus and Jortner–Bixon models. In particular, our model includes a quantum vibration as in Jortner–Bixon theory, a classical vibration as in Sumi–Marcus theory, and the classical solvent present in both theories. Using this model, we were successful in making accurate rate predictions in both fast and slow solvents. This paper presents further time–resolved, variable–wavelength, pump–probe data on betaine in several solvents and a further investigation of the hybrid model, including some of the spectral consequences of this type of diffusive model. Section II describes the experimental apparatus used in the pump–probe measurements. Section III summarizes the previous data, presents the new experimental data, and provides a qualitative interpretation. Section IV describes the hybrid model in detail and presents simulated, time–resolved spectra. Some of the main findings about the model are: 1) nonexponential electron–transfer kinetics can lead to exponential spectral kinetics (within the accuracy of the calculation), even measured near the absorption band maximum; 2) inductive electron–transfer behavior (the rate is small at early times and accelerates due to nuclear relaxation in the excited state) in fast solvents can be masked in the transient spectra by transient–Stokes–shifting phenomena; 3) motion of population in the excited state can lead to a transient increased absorption on the low–energy edge of the absorption band following charge transfer; and 4) different initial population distributions can lead to vastly different spectral kinetics. Section V compares experimental data with the predictions of the model and discusses the shortcomings and approximations of the model in light of the comparison. Special attention is given to the possible consequences of an inertial component in solvation dynamics and to the assumption of instantaneous vibrational relaxation. Finally, the conclusions are presented in Section VI.

II. EXPERIMENTAL METHODS

Most of the time–resolved experiments presented in this paper were performed using a femtosecond dye laser amplified by the output of a Nd:YAG regenerative amplifier, as shown in Figure 1. An acoustooptically modelocked Nd:YAG laser produced a train of 100 ps pulses at 76 MHz. Most of the light was doubled in KTP and used to synchronously pump the dye laser. A small fraction of the light was used to seed the Nd:YAG regenerative amplifier. The output from the dye laser was amplified in 3 flowing dye cells by the doubled output of the Nd:YAG regenerative amplifier. This light was then used for the experiments.

Our regenerative amplifier is based on the designs of Nelson[17] and Dlott,[18] with cavity modifications to match the thermal lensing that occurs in our Nd:YAG rod. The cavity is an acoustooptically Q–switched, electrooptically cavity dumped, continuously pumped Nd:YAG laser built around a Quantronix 116 head. An antireflection–coated glass plate following the output coupler of the modelocked Nd:YAG laser was used to remove a small fraction of the light for reamplification in the Nd:YAG regenerative amplifier. This low–intensity pulse train from the modelocked Nd:YAG passed through crossed polarizers surrounding a $LiNbO_3$ crystal, which was used to electrooptically select single "seed" pulses at 500 Hz. Because the Nd:YAG regenerative amplifier reached saturation, switching the full $\lambda/2$ voltage on the $LiNbO_3$ crystal was unnecessary. The selected pulses passed through a lens, which served to match the size and divergence of the seed beam to the beam size and divergence of the regenerative amplifier for more efficient injection. Injection was achieved acoustooptically by Bragg diffraction through the Q–switch.[18] The seed pulse arrived at the Q–switch after the RF driving field had been stopped but before complete relaxation of the acoustic wave in the crystal. Because the acoustic wave still had some amplitude, the seed pulse was Bragg diffracted into the cavity. The seed pulse was selectively amplified and then electrooptically ejected, yielding 1.0–1.2 mJ pulses at 1064nm. These pulses were frequency doubled in KTP with ≃50% efficiency.

The major fraction of the output from the modelocked Nd:YAG passed through an acoustooptic modulator (IntraAction), which was used to remove amplitude fluctuations. The light was frequency doubled in KTP. A small fraction of the resultant green light was directed onto a photodiode to provide the error signal that was applied to the acoustooptic modulator. Using this scheme, amplitude fluctuations of the 532 nm light were less than 0.1% in the 0 Hz–40 kHz regime.

The amplitude–smoothed 532 nm pulses were used to synchronously pump a 5–mirror, 2–jet, linear dye laser that does not contain prisms. The gain medium was Styryl 8 and the saturable absorber was HITCI. The output of the dye laser, when pumped at threshold, was several milliwatts of ≃150 fs pulses near 800 nm. When pumped above threshold, the pulses developed wings and satellites. This performance was recently improved (≃70 fs) by switching to a different mirror set and a 6–mirror cavity design.

The dye–laser output was amplified in a 3–stage dye amplifier pumped by the output of the regenerative amplifier. All three stages used flow cells containing Styryl 8 in propylene carbonate. The first two stages were single–pass 1 mm cells with focusing of the green and the red. The third stage was a double–pass 10 mm cell with mild focusing of the green pump beam. Double passing was achieved by placing a high reflector for normal incidence at 800 nm as close to the cell as physically possible and pumping through the high reflector. This double passing gave an extra factor of 2–3 in amplification. Coarse timing of the amplifier was achieved using a fixed optical delay line. Exact timing was achieved by varying the cavity length of the regenerative amplifier. Because the timing is optical rather than electronic, there was no timing drift as there is in copper vapor laser or Q–switched Nd:YAG pumped amplifiers. The output from the amplifier has been as high as 16 μJ/pulse although 10–12 μJ/pulse was more common.

The output power from the dye amplifier was sufficient to perform pump–probe spectroscopy that required nonlinear generation of light, including frequency doubling or continuum generation. One common configuration is shown in Figure 2. Twenty percent of the light was split off for the pump and the rest was used to generate continuum in H_2O A portion of the continuum was selected with a 10 nm interference filter and reamplified in a dye cell pumped by some of the 532 nm output from the regenerative amplifier. We have also performed one–color continuum pump/continuum probe experiments at 700 nm and 600 nm by using all of the light to generate continuum and reamplifying the continuum in 2 stages to the 0.2 μJ/pulse and 2 μJ/pulse energy level for 700 nm and 600 nm, respectively. Some experiments on betaine in alcohols used independently tunable pump and probe light. In this case, all of the amplified dye laser light was used for continuum generation. The continuum was split into two beams, which were independently spectrally filtered and amplified. The probe was amplified in one dye cell and the pump was amplified in two dye cells.

After generation of pump and probe pulses, the pump beam was chopped at 250 Hz, blocking every other pulse. One beam was passed through a variable delay and the other was passed through a fixed delay. Both beams were focused into the sample, and the probe was detected. Probe and reference beams were adjusted to have equal intensities in the absence of the excitation beam. Both signals were amplified in boxcars (Stanford Research Systems SR250) and subtracted. (Subtraction was used as an approximation to division, which is valid for small signals and equal probe and reference levels in the absence of pumping.) The difference signal was the input to a third boxcar operated in toggle mode (successively adds and subtracts every other shot) to give the change in transmission upon excitation by the pump beam. The maximum change in transmission caused by the pump was 1% of the total transmission. The sensitivity of the system is better than 10^{-4}.

Betaine in toluene data were taken on a Ti:sapphire–based, ultrafast, pump–probe spectrometer, which is described in detail elsewhere.[19] In this system, 90 fs pulses were generated by a Kerr–lens–modelocked Ti:sapphire oscillator. These pulses were stretched to ≈ 120 ps using a grating stretcher, amplified at 2 kHz in a Ti:sapphire regenerative amplifier, and temporally recompressed. The resultant light consisted of 130 fs pulses centered at 780 nm with 200 μJ per pulse. For these experiments, 60 μJ in a several millimeter spot were used for pumping the sample and 140 μJ were used to generate continuum in quartz for probing.

Static absorption spectra were taken on either a Shimadzu UV160 or a Cary 17 absorption spectrometer. All solvents were either of spectrophotometric or HPLC grade. Some of the nonpolar solvents were dried over activated alumina prior to use. Betaine–30 was purchased from Aldrich and used as received.

III. EXPERIMENTAL RESULTS AND DISCUSSION

We have made extensive new pump–probe measurements on betaine in a variety of solvents with tunable pump and probe wavelengths. The results are consistent with the previously reported measurements[1–3] following excitation into S_1 and S_3. The $S_0 \to S_1$ absorption in the visible to the near–infrared region of the spectrum corresponds to a charge transfer absorption band.[20] The position of this band (which is the basis for the $E_T(30)$ empirical polarity scale[20]) is a strong function of solvent polarity, appearing at higher energy in more polar solvents. Excitation of this band causes an electron to move from the phenolate ring to the pyridinium ring, Scheme 1. We previously reported reverse electron transfer rates (pyridinium→phenolate) obtained by single color pump–probe spectroscopy in a variety of solvents, as summarized in Table 1.[1,2]

In contrast to the $S_0 \to S_1$ absorption band, the $S_0 \to S_3$ absorption band does not shift with solvent polarity, indicating that the S_3 state has approximately the same dipole moment as the ground state. We previously determined that $S_0 \rightarrow S_3$ excitation was followed by an extremely fast (<200 fs in all solvents studied) $S_3 \rightarrow S_1$ internal conversion.[3] This fast internal conversion was followed by a slower $S_1 \rightarrow S_0$ internal conversion, which occurred on the same time scale as the $S_1 \rightarrow S_0$ internal conversion following optical preparation of the S_1 state.[3]

Most of the previously reported data followed excitation into S_1 and were recorded at a single probe and a single pump wavelength. Because the absorption band position is a function of solvent polarity, experiments in different solvents probed different regions of the absorption band. From the previous data, it is difficult to evaluate the possibility that selective excitation out of an inhomogeneous distribution contributes to the observed differences in different solvents. Also, extraction of electron–transfer times is complicated by contributions to the observed dynamics from band shifting following the electron transfer. To address these issues, we have performed variable wavelength pump–probe experiments on betaine, the results of which are reported here.

Figures 3–8 show the strongly diverse dynamics that are observed upon changing the solvent, pump wavelength, and probe wavelength. Each plot shows the change in absorbance caused by the pump pulse (ΔOD) as a function of delay time between the pump and probe pulses. A positive signal corresponds to a pump–induced absorption and a negative signal corresponds to a pump–induced stimulated emission and/or bleach.

Following excitation of the charge transfer band ($S_0 \rightarrow S_1$), we observe dynamics that depend strongly on probe wavelength and solvent, Figures 3–6. The initial sign of the signal depends on probe wavelength. At long wavelengths we observe a negative signal (bleach of the $S_0 \rightarrow S_1$ absorption and/or stimulated emission, $S_1 \rightarrow S_0$), and at short wavelengths (640nm and shorter) we observe an excited state absorption ($S_1 \rightarrow S_n$). The alcohols have no absorption at 790 nm at room temperature so the initial negative signal (Figure 6, 1–propanol) must be due to stimulated emission. In most cases, however, we believe that the major contribution to the negative signal at late times is a bleach and we will refer to a negative signal as a bleach for the rest of this discussion.

The observed signals depend on the relative pump and probe polarization. The initial bleach is larger for parallel polarizations than for perpendicular polarizations as expected when pumping and probing the same transition. However, the initial absorption is larger for perpendicular polarization than for parallel polarization indicating that the transition dipole moment of the $S_1 \rightarrow S_n$ absorption points in a different direction than that for $S_0 \rightarrow S_1$.

The sign of the signal at long time depends on the position of the probe wavelength relative to the absorption maximum of betaine in that particular solvent. The signal is an absorption at probe wavelengths longer than the absorption maximum and a bleach at probe wavelengths shorter than the absorption maximum. The polarization dependence of the long time component is the same as the polarization dependence of the initial bleach at longer probe wavelengths, indicating that this signal is associated with the $S_0 \rightarrow S_1$ transition. As we will show in Sections IV–V, this late time behavior is consistent with energy deposition into nuclear degrees of freedom of the solute and solvent.

The late–time band shifting is minimized near the absorption maximum. Table 2 lists bleach recovery times measured near the absorption maximum in various solvents, which we assign to the electron transfer times. In several cases, these electron transfer times are longer than the previously reported electron transfer times listed in Table 1 because most of the previous data were obtained on the red edge of the absorption spectrum and therefore, were complicated by band–shifting. We have also extended our solvent dependent studies to include several alcohols. These results, listed in Table 3, are consistent with our previous interpretation[1–3] that the electron transfer rate becomes independent of solvation dynamics in slowly relaxing solvents.

The dynamics do not seem to be a strong function of pump wavelength when exciting in the charge–transfer band and probing near the absorption maximum, Table 4.

The dynamics at late time also seem to be independent of pump wavelength following excitation to S_1 or S_3 and probing in S_3.[3] However, there is a significant difference in behavior between S_1 and S_3 excitation when probing at the low–energy edge of the $S_0 \rightarrow S_1$ absorption band. In acetone, the sign of the initial signal is different (Figure 7). In glycerol triacetate (GTA) the bleach recovery is faster and the relative size of the late time absorption is much larger following S_3 excitation (Figure 8). This pump–wavelength dependence is also consistent with energy deposition, see below.

IV. SIMULATION OF TRANSIENT–ABSORPTION SPECTRA

To simulate the time dependence of the ΔOD spectra, we must consider the population dynamics in the ground and excited states, including both motion upon the excited and ground state surfaces and transitions between the two surfaces. At any given time after excitation, the population that is "missing" from the ground state due to the excitation contributes a bleach signal to the ΔOD spectrum. The population in the excited state at that time contributes to the ΔOD spectrum by absorption to higher excited states ($S_1 \rightarrow S_n$) and stimulated emission to the ground state. Because we do not have a good estimate for the shape or the oscillator strength of the $S_1 \rightarrow S_n$ transition, we will only model the bleach and stimulated emission signals. This section presents calculations of time–resolved ΔOD spectra for betaine in acetone and GTA. These two solvents were chosen as representative solvents with similar polarities[20] (as measured by the $E_T(30)$ polarity scale) but very different solvation times.[21] The model used is an extension of an inhomogeneous model for electron transfer that was previously used by Walker *et al.*[3] to predict the electron–transfer dynamics in betaine. All parameters used were obtained independently and were not adjusted in these simulations. Therefore, comparison of the predicted results with the experimental results provides an unambiguous assessment of the strengths and weaknesses of the model.

The Walker *et al.* Model.

The Walker *et al.* model[2] includes two vibrational modes, a quantum mode to act as an energy accepter for inverted–regime electron transfer[1–5,10,16,22] and a classical mode to drive the electron transfer in the absence of solvent fluctuations.[1,2,9] The third degree of freedom in the model is an overdamped classical coordinate that represents the solvent.[1,2,9,10,12,13,21] All three degrees of freedom contribute to the reaction dynamics in varying amounts depending on the electron transfer system being studied. Electron transfer to an upper level of the quantized vibrational mode of the product state can greatly reduce the barrier to reaction, increasing the rate in the inverted regime. Fluctuations of the solvent polarization can be rate limiting when the vibrational barrier is small. These fluctuations equalize the energy levels between the two states, driving the reaction with a rate proportional to $1/\tau_s$, where τ_s is the correlation time for the polarization fluctuations, often called the solvation time.[21] Low–frequency vibrations, the classical vibration in this model, can also drive the reaction in nonpolar solvents and in polar solvents with very slow solvation dynamics (τ_s very large).

In the Walker *et al.* model, as in Sumi–Marcus theory,[9] the electron transfer occurs along the vibrational coordinates with a rate, k(X), that is a function of the solvent coordinate, X. Motion of the classical population distribution along X in the excited state, $P_e(X,t)$, and population transfer from the excited state to the ground state (electron transfer) are described with a classical reaction–diffusion equation:

$$\frac{\partial P_e(X,t)}{\partial t} = D\,\frac{\partial^2 P_e(X,t)}{\partial X^2} + \frac{D}{k_B T}\,\frac{\partial}{\partial X}\left[P_e(X,t)\,\frac{\partial V_e}{\partial X}\right] - k(X)P_e(X,t). \qquad (1)$$

We have added a second reaction–diffusion equation to describe the appearance and motion of the classical population distribution on the ground state, $P_g(X,t)$:

$$\frac{\partial P_g(X,t)}{\partial t} = D\frac{\partial^2 P_g(X,t)}{\partial X^2} + \frac{D}{k_BT}\frac{\partial}{\partial X}\left[P_g(X,t)\frac{\partial V_g}{\partial X}\right] + k(X)P_e(X,t). \tag{2}$$

Both have the same diffusion constant, $D=(k_BT)/(2\lambda_{solv}\tau_s)$, where λ_{solv} is the solvent reorganization energy.

The X–dependent rate can be expressed as a sum over rates to different vibronic states, n, of the ground electronic state,

$$k(X) = \sum_n k_{NA}^{0\to n}(X) \tag{3}$$

where $k_{NA}^{0\to n}(X)$ is the nonadiabatic rate constant,

$$k_{NA}^{0\to n}(X) \propto V_{el}^2 \, |\langle 0|n\rangle|^2 \exp(-\Delta G_{0\to n}^{\ddagger}/k_BT). \tag{4}$$

Here, V_{el} is the electronic matrix element and $|\langle 0|n\rangle|^2$ is the Franck–Condon factor for the quantized vibration. $\Delta G_{0\to n}^{\ddagger}$ is the barrier to the nth vibrational level of the ground state and depends on the quantized mode and both classical modes:

$$G_{0\to n}^{\ddagger} = (\lambda_{solv}+\Delta G^{\circ}-2X\lambda_{solv}+nh\nu_{QM}+\lambda_{cl,vib})^2/(4\lambda_{cl,vib}). \tag{5}$$

Here, ν_{QM} is the frequency of the quantized vibration and $\lambda_{cl,vib}$ is the reorganization energy of the classical vibration. Since electron transfer in betaine occurs in the inverted regime, electron transfer to an excited vibrational level of the ground state involves a smaller barrier, and therefore a faster rate than electron transfer to n=0. Also, the barrier depends on X, and solvent motion can therefore increase the rate.

It is important to note that each vibronic transition in the hybrid model acts like a Gaussian sink with a width proportional to $\lambda_{cl,vib}$. Electron transfer can therefore occur in the absence of solvent relaxation. In contrast, in Jortner–Bixon theory[10] the vibronic transitions act as delta–function sinks. Therefore, in the absence of solvent relaxation, there is no mechanism to equalize the energy levels and electron transfer cannot occur for most solvent configurations. In fact, in the low barrier limit, Jortner–Bixon theory predicts that the rate is proportional to $1/\tau_s$. In the Walker *et al.* model, as in Sumi–Marcus theory,[9] the rate can exceed $1/\tau_s$, as has previously been observed experimentally for betaine in GTA.[1,2]

To obtain the parameters used in the kinetic model, we fit the measured absorption lineshape to a model that includes two nuclear degrees of freedom, one classical and one quantized.[2,14] From this fit, we obtain the reorganization energies for the two degrees of freedom, λ_{cl} and λ_{QM}, the free energy gap, ΔG^o, and the frequency of the quantum mode, ν_{QM}. λ_{cl} is partitioned into the solvent and vibrational portions by assuming that $\lambda_{cl}=\lambda_{cl,vib}$ in cyclohexane. λ_{solv} in any other solvent is then equal to the difference between λ_{cl} (measured in that solvent) and $\lambda_{cl,vib}$ (from cyclohexane). V_{el} is estimated from the Hush relationship[23] (1400cm^{-1} for betaine–30 assuming that the distance the electron is transferred is equal to the prediction of a valence bond description as in Scheme 1). The parameters for betaine–30 in acetone and GTA are summarized in Table 5.

Implicit in the preceding discussion is the assumption of instantaneous relaxation of both the quantized and classical vibrational modes. Because these relaxations occur instantaneously, there is no back reaction within this model. In contrast to the vibrational degrees of freedom, the solvent bath has a finite relaxation rate. Because the electron transfer rate is a function of X, the initial population distribution along the solvent coordinate, $P_e(X,t=0)$, and its subsequent evolution can strongly influence the dynamics. For the simulations presented here, we studied two limits, selective and broadband excitation.

Broadband Excitation Simulations

For broadband excitation simulations, we used the equilibrium ground–state distribution along X for the zero–time excited state probability distribution, $P_e(X,t=0)$. Figure 9a shows the free energy curves for the electron transfer in acetone. Figures 9b and 9c show the time dependence of the ground– and excited–state population distributions for acetone following broadband excitation. At t=0, there is a Gaussian distribution centered at X=1 in the excited state and no population in the ground state. In the excited state, the population solvates towards lower energy (X=0) and decays due to the electron transfer. In the ground state, the population appears near X=0 due to electron transfer and then solvates back towards X=1. Note that at intermediate times, the ground–state population near X=0 is greater than the equilibrium population there. As will be shown later, this situation leads to an increased absorption.

Figure 10 shows the ground– and excited–state population distributions for GTA, again assuming broadband excitation. As before, at t=0, there is a Gaussian distribution centered at X=1 in the excited state and no population in the ground state. In this case, however, we observe very little motion along X in the excited state. In fact, the population appears to be shifting towards higher energy. This shifting is an illusion, however, due to the strongly inhomogeneous electron transfer kinetics: molecules whose solvent configuration is more favorable for reaction (closer to X=0) react faster. Examination of the ground–state dynamics shows that there is a small amount of shifting due to solvation dynamics. As in acetone, there is excess population at lower X, indicating that the solvent is being displaced slightly during the course of the reaction. However, solvent motion is certainly not driving the electron transfer as it does in acetone.

We can calculate the transient spectrum as a function of time, $TS(\nu,t)$, by convoluting the time–dependent ground– and excited–state population distributions with a vibrational shape function. The missing ground–state population contributes to a bleach band, $TS_b(\nu,t)$. The excited–state population contributes to a stimulated emission band,

$TS_s(\nu,t)$, which is vibrationally Stokes shifted from the bleach because we have assumed instantaneous vibrational relaxation. The vibrational shape function is a series of lines arranged in the Franck–Condon progression for a harmonic oscillator with frequency ν_{QM} and reorganization energy λ_{QM} appropriately directed for the bleach band or the stimulated emission band. The vibronic lines are modeled as Gaussians with widths corresponding to a Boltzmann distribution in the classical vibrational coordinate.

Figure 11 shows $TS_s(\nu,t)$, $TS_b(\nu,t)$, and $TS(\nu,t)$ $(\equiv TS_s(\nu,t)+TS_b(\nu,t))$ for acetone. The stimulated emission band, shown in Figure 11a, shifts to lower energy due to solvation dynamics and decreases in amplitude due to the electron–transfer reaction. The bleach band, shown in Figure 11b, recovers and then changes sign to become an absorption on the low energy edge due to reaction. Subsequently, solvation dynamics redistributes the population to recover the equilibrium spectrum. Figure 11c shows the full spectrum as a function of time. From this spectrum, it is apparent that the observed dynamics will be a strong function of probe wavelength. Dynamics at the red edge of the stimulated emission band reflect motion of the population in the excited state and the charge transfer. Dynamics observed in the region between the two bands reflect a complicated combination of dynamics, from both excited–state and ground–state solvation as well as the electron transfer. Dynamics near the peak of the bleach band show the smallest contribution from solvation dynamics and are most representative of the electron–transfer dynamics. Dynamics at the blue edge of the bleach band are due to both the charge transfer and solvation dynamics in the ground state.

Figure 12 shows $TS_s(\nu,t)$, $TS_b(\nu,t)$, and $TS(\nu,t)$ for GTA. In this case, the bands shift very little due to solvation dynamics during the course of the reaction because the electron transfer is much faster than solvation dynamics in GTA. The major contribution to the spectral dynamics is the electron transfer reaction. The stimulated emission band, shown in Figure 12a, shifts slightly, and there is a slight increased absorption on the red edge of the bleach band as seen in Figure 12b. The total spectral dynamics, Figure 12c, are not a strong function of probe wavelength, in contrast to acetone.

Selective Excitation Simulations

We have studied the effect of selective optical excitation, or spectral hole burning, on the kinetics. The excitation pulse was modeled with a Gaussian frequency profile centered at a chosen wavelength with a 10 nm width and a variable intensity. We calculated $P_e(X,t=0)$ by projecting out population in S_0 as a function of X; the probability of absorption at any X is a function of the energy gap, the vibrational shape function, and the excitation intensity. The figures presented here all used the same arbitrary excitation intensity. $P_g(X,t=0)$ is the difference between the equilibrium ground–state distribution function, $P_g(X,t=\infty)$, and $P_e(X,t=0)$.

Figure 13 shows the ground– and excited–state population dynamics for betaine in acetone using selective excitation assuming a center wavelength of 700 nm. In the excited state, Figure 13a, the initial population distribution is broad, although it is narrower than the width of the distribution obtained under broadband excitation conditions, Figure 9a. As in the broadband excitation case, the initial distribution solvates towards lower energy and then undergoes electron transfer. In the ground state, Figure 13b, the population hole broadens with time due to solvation and is subsequently filled in by reaction. As in the broadband excitation case, there is excess population in the ground state near X=0 at intermediate times, which leads to an increased absorption, as seen in Figure 14, which shows the transient spectrum for acetone assuming 700 nm excitation.

Although the qualitative features are similar, the details differ for broadband and selective excitation. The total electron–transfer dynamics under different excitation conditions can be conveniently compared using the survival probability, S(t), which is the total population in the excited state at time t divided by the total population at t=0:

$$S(t) = \frac{\int P_e(X,t)\, dX}{\int P_e(X,0)\, dX}. \qquad (6)$$

Figure 15 shows S(t) for betaine in acetone assuming broadband excitation and selective excitation at 800 nm, 700 nm, and 640 nm. In all four cases, there is an induction period at early time during which the electron–transfer rate is very small. This delay is followed by an acceleration of the rate. The induction period corresponds to the period of time during which excited–state solvation is occurring prior to the electron transfer. The contribution of the induction period to the dynamics is smallest at 800nm excitation because the initial population distribution has a smaller average energy gap than the other initial population distributions. Despite the differences in the induction period, the long–time dynamics are quite similar. Since solvation dynamics move the population to the region of the free energy surface where electron transfer effectively competes with solvation, the rate coefficient, k(t), defined as

$$k(t) = \left. \frac{dS(\tau)}{d\tau} \right|_t \tag{7}$$

becomes independent of the initial solvent configuration for $t >> \tau_S$.

Figure 16 shows S(t) for betaine in GTA assuming broadband excitation and selective excitation at 800 nm, 700 nm, and 640 nm. For GTA, there is no obvious induction period or an acceleration of the rate at later times; the reaction occurs through the vibrational channels near the initially excited solvent positions. Because of the strongly inhomogeneous electron–transfer kinetics, the late–time dynamics vary considerably under different excitation conditions and the population decays are nonexponential. Interestingly, the spectral dynamics at the absorption maximum are not very sensitive to the inhomogeneous kinetics. This result implies that it is difficult to experimentally study hole burning effects in the present measurements, see below.

We have also investigated the influence of different excitation intensities on the spectral dynamics. With increasing intensity, the differences between different excitation wavelengths decrease until, at high enough intensity, the broadband excitation limit is reached. Conversely, decreasing the excitation intensity increases the excitation wavelength dependence of the calculated dynamics.

V. COMPARISON OF EXPERIMENT AND THEORY

From the spectral simulations, we can obtain absorption–transients that are directly comparable to the experimental data by calculating the time–dependent absorption changes at specific wavelengths and convolving these calculated signals with an experimental instrument response function. This procedure allows us to determine the initial conditions that best represent the experiment. We are also able to quantitatively evaluate various predictions of the model, including the presence or absence of an induction period, the degree of inhomogeneous spectral kinetics, and contributions to the spectral dynamics from energy deposition into the solvent polarization. Such comparisons highlight the strengths and limitations of the model.

Figure 17 compares simulated (broadband excitation) and experimental transients for GTA at several probe wavelengths. The agreement is remarkable, especially since we used *no adjustable parameters* in making these predictions: all parameters were obtained from static absorption spectra of betaine[2] and from independent measurements of solvation dynamics in the relevant solvents.[21] The model predicts the main qualitative features, including the long–time increased absorption at 800 nm and the two–component bleach recovery at 640 nm. At 700 nm and 640 nm the agreement is almost quantitative. At 800 nm, the observed bleach recovery is faster than the predicted recovery. This discrepancy may be caused by the assumption of instantaneous vibrational relaxation in the simulations, see below.

Figure 18 compares the observed and predicted (broadband excitation) transients in acetone. The model predicts the main features of the observed spectral dynamics, including faster bleach recovery at lower energy and the increased absorption at 800 nm. However, the model predicts inductive behavior at 700 and 640 nm, which was not observed experimentally. The model also predicts the wrong amplitude and decay rate for the increased absorption at 800 nm. These failures of the model may also be caused by the assumption of instantaneous vibrational relaxation, see below.

Surprisingly, the experimental and simulated transients in GTA are both exponential near the absorption maximum (700 nm), even though the survival probability was predicted to be nonexponential. Also, there is not a strong variation with probe wavelength for the predicted and observed transients, as might be expected for inhomogeneous electron transfer. Apparently, the observed spectral dynamics reflect the average electron transfer kinetics rather than the inhomogeneous details, because, in the case of betaine, the vibrational contribution to the width of the absorption spectrum is larger than the solvent contribution to the width.

Experimentally, we did not observe an excitation wavelength dependence of the kinetics, as seen in Table 4. For acetone, this result might be expected because the reaction is driven by solvation dynamics. This observation is somewhat surprising, however, for GTA, which according to the model should show an excitation wavelength dependence in the case of selective excitation (Figure 16). This discrepancy between experiment and simulation may be due to high excitation intensities and/or the assumption of a single solvent relaxation time. High excitation intensities can cause the system to behave in the broadband excitation limit. Fast solvent relaxation times, relative to the instrument response function, can redistribute population in the ground state during the excitation process and, thereby, "wash out" the photoselection effect.

The Effects of Vibrational Relaxation

In acetone, the model predicts an induction period at probe wavelengths of 700 and 640 nm but no induction at 800 nm (Figure 18). There is no predicted induction at 800 nm because the early–time dynamics in acetone at 800 nm are dominated by the shifting of the stimulated emission band, see Figure 11. In calculating the dynamics, we assumed instantaneous vibrational relaxation; that is, at t=0, the stimulated emission band was assumed to be vibrationally Stokes shifted. Immediately after excitation, however, the stimulated emission band should reflect the degree of vibrational excitation in the excited state. Then, through vibrational relaxation and solvation dynamics, the stimulated emission band will shift to its equilibrium position. Adding a rapid but finite vibrational relaxation (rather than an instantaneous vibrational relaxation) to the model would "wash out" the predicted inductive kinetics at higher energy by introducing a time–dependent vibrational Stokes shift component to the dynamics at higher energies.

Adding excited–state vibrational relaxation to the model could also help to rectify the differences between experiment and theory for GTA. An excited–state vibrational relaxation that is faster than the electron–transfer rate would cause a faster decay at 800 nm. Therefore, solvent relaxation and vibrational relaxation are both necessary for the description of the observed dynamics in GTA. Vibrational relaxation gives the accelerated dynamics and solvent relaxation yields the long–lived increased absorption.

The difficulty in predicting the correct amplitude and relaxation time of the increased absorption at 800 nm in acetone could also be rectified with a more realistic treatment of vibrational relaxation. Slow vibrational relaxation in the ground state would increase the recovery time and change the predicted amplitude of the increased absorption. This idea is consistent with the observation of energy deposition in toluene, where heating of the solvent coordinate should be quite small due to the small solvent reorganization energy for a nonpolar solvent. In some sense, the model emphasizes heating in the wrong degree of freedom. During solvent relaxation in the excited state, λ_s (=1881 cm^{-1} for acetone) is deposited into the solvent. Because excitation occurred with a 12,500 cm^{-1} photon, much more energy must be deposited into intramolecular modes of the solute than into specific excitation of the solvent polarization.

Table 6 lists the recovery times of the late–time absorption observed on the red edge at nearly equal shifts from the absorption maximum in several solvents. The size of this late–time absorption is a measure of the energy deposition and therefore the absorption recovery time is a measure of the local cooling time. The cooling in toluene is slower than the cooling in acetone and benzonitrile but much faster than that in GTA and the alcohols. This variation of cooling rates as a function of solvent can be understood if we assume that energy deposition and cooling involving intramolecular degrees of freedom occurs in both polar and nonpolar solvents. The cooling observed in nonpolar solvents reflects exclusively intramolecular cooling. The cooling in polar solvents, however, has contributions from both intramolecular cooling and relaxation of the nonequilibrium solvent polarization. τ_S for acetone and benzonitrile is faster than the intramolecular cooling time (the cooling time in toluene), so the total rate cooling is faster than the rate in toluene. Conversely, τ_S for GTA and the alcohols is much slower than the intramolecular cooling time, so the rate of total cooling is slower.

The dynamics observed following excitation of the S_3 band are also consistent with energy deposition into intramolecular modes of the solute. Following excitation at 400 nm, twice as much electronic energy is converted into nuclear energy than in the case of 800 nm excitation. This additional energy leads to a much larger shift in the transient–absorption spectrum and a much larger observed absorption at a probe wavelength of 800 nm. The additional 12,500 cm^{-1} of energy must go into intramolecular nuclear degrees of freedom because S_0 and S_3 have similar dipole moments[3] so that the poulation distribution created along the solvent coordinate in S_1 is similar whether it is created optically ($S_0 \rightarrow S_1$) or by internal conversion ($S_3 \rightarrow S_1$). In acetone, the absorption is so large that we no longer observe a bleach at early times, only an increased absorption that decays on the same time scale as the increased absorption observed when pumping at 800 nm, see Figure 7. In GTA, we still observe the bleach, but the size of the increased absorption is much larger and recovers faster, see Figure 8. The dynamics observed in benzene following excitation at 400 nm show a bleach but no increased absorption because 800 nm is very close to the absorption maximum in benzene, so the effects of energy deposition are minimized here.

The Effects of an Inertial Component in Solvation Dynamics

We have investigated the possible effects of an inertial component of the solvent response on the predicted dynamics. Inertial effects in solvation dynamics have been predicted by molecular dynamics simulations[24,25] and were recently observed experimentally.[26] We crudely simulated an inertial component of a given magnitude (%Inertial) by further partitioning the solvent reorganization energy, λ_{solv}, into an instantaneously relaxing portion, λ_{fast}, and a slowly relaxing diffusive portion, λ_{slow}. λ_{fast} roughly represents the inertial contribution to the solvation energy. Table 7 lists survival probabilities as a function of the size of the inertial component. The two survival probabilities are defined as[9]

$$\tau_a = \int S(t)\, dt \tag{8}$$

and

$$\tau_b = \int t\, S(t)\, dt. \tag{9}$$

τ_a is most sensitive to early time dynamics while τ_b is more sensitive to late time dynamics. $\tau_a < \tau_b$ indicates a distribution of rates arising from an inhomogeneous distribution. When $\tau_a \approx \tau_b$, the electron–transfer dynamics can be reasonably well represented by a single exponential decay. $\tau_a > \tau_b$ indicates an acceleration of the rate due to solvent relaxation following an induction period during which the rate is slow.

The tabulated numbers indicate that an inertial component of considerable size would be supported within this model for acetone but not for GTA. The inertial dynamics diminish the predicted induction in acetone, bringing the theoretical predictions into closer agreement with experiment. In GTA, however, there is no predicted induction so the added inertial component serves to accelerate the electron transfer rates to values that are not in agreement with experiment. Acetone probably does have a much larger inertial component than GTA because of the very large mass of GTA.

Spectral simulations performed assuming an inertial component also show the same qualitative features as the simulations discussed above, including specific heating of the solvent coordinate (see Figure 19, which compares TS(ν,t) in acetone for %Inertial values of 20%, 40%, 60%, and 80%). The major differences for %Inertial values ranging from 0% to 60% are the contribution of the induction and the relative amplitude of the increased absorption. At %Inertial = 80%, the model predicts an increased absorption at all wavelengths probed experimentally. Thus, we conclude that the model is consistent with an inertial component as large as 60% for acetone but is not consistent with any inertial component in GTA. For comparison, the Fleming group has reported experimental observations of an inertial component of 80% for acetonitrile[26] and molecular dynamics simulations by Fonseca and Ladanyi predict an inertial component of 20% for methanol.[25]

VI. CONCLUSIONS

We have measured the electron–transfer dynamics of betaine in polar and nonpolar solutions. The rate is controlled by solvation dynamics in rapidly relaxing polar solvents. However, the electron transfer can be faster than solvation dynamics in slowly relaxing solvents and also occurs in nonpolar solvents, indicating the importance of intramolecular vibrations in promoting the reaction. In addition to the electron–transfer kinetics, we have observed evidence for energy deposition into nuclear degrees of freedom following the charge transfer in polar and nonpolar solvents. The observed heating is almost certainly caused by energy deposition into intramolecular modes in nonpolar solvents. In polar solvents, however, the observed heating reflects energy deposition into intramolecular modes and the solvent polarization, both of which can be displaced in the excited state prior to electron transfer. The relative contribution of the two heating mechanisms to the spectral dynamics in polar solvents is a function of the electron–transfer time, the solvation time, and the vibrational cooling time. For solvents in which the electron–transfer time and the solvation time are slower than the vibrational cooling time (GTA and the alcohols), the observed cooling dynamics are primarily due to displacement of the solvent polarization. In faster solvents, the observed cooling dynamics are due to energy deposition in both the solvent polarization and intramolecular modes.

We have modeled the dynamics using a diffusive model for the reaction. This model predicts the electron–transfer dynamics and some of the local heating, due to displacement along the solvent coordinate following reaction, giving an indication of the partitioning of energy into the various nuclear degrees of freedom following the electron transfer. A more complete description would include vibrational relaxation and inertial components of the solvation dynamics. These effects could diminish the predicted induction in acetone. Vibrational relaxation could lengthen the lifetime of the predicted increased absorption in acetone and recover the spectral inhomogeneity in GTA.

ACKNOWLEDGEMENTS

This research was funded by the Office of Naval Research. NEL and DAVK were supported as National Science Foundation Postdoctoral Fellows. We would also like to thank Dr. G.C. Walker for helpful discussions.

REFERENCES

1. E. Akesson, G.C. Walker and P.F. Barbara, J. Chem. Phys. 95 (1991) 4188.
2. G.C. Walker, E. Akesson, A.E. Johnson, N.E. Levinger and P.F. Barbara, J. Phys. Chem. 96 (1992) 3728.
3. N.E. Levinger, A.E. Johnson, G.C. Walker and P.F. Barbara, Chem. Phys. Lett. 196 (1992) 159.
4. G.C. Walker, P.F. Barbara, S.K. Doorn, Y. Dong and J.T. Hupp, J. Phys. Chem. 95 (1991) 5712.
5. K. Tominaga, D.A.V. Kliner, A.E. Johnson, N.E. Levinger and P.F. Barbara, J. Chem. Phys. 98 (1993) 1228.
6. K.E. Schultz, D.J. Russell and C.B. Harris, J. Chem. Phys. 97 (1992) 5431.
7. J. Rodriguez and D. Holten, J. Chem. Phys. 91 (1989) 3525.
8. For a discussion of solute vibrational hot bands see: T. Elsaesser and W. Kaiser, Annu. Rev. Phys. Chem. 42 (1991) 83.
9. H. Sumi, and R.A. Marcus, J. Chem. Phys. 84 (1986) 4894.
10. J. Jortner, and B. Bixon, J. Chem. Phys. 88 (1988) 167.

11. A.I. Burshtein and A.G. Kofman, Chem. Phys. 40 (1979) 289; L.D. Zusman, Chem. Phys. 49 (1980) 295; D.F. Calef and P.G. Wolynes, J. Phys. Chem. 87 (1983) 3387; B. Bagchi, G.R. Fleming and D.W. Oxtoby, J. Chem. Phys. 78 (1983) 7375; N. Agmon and J.J. Hopfield, J. Chem. Phys. 78 (1983) 6947; N. Agmon and J.J. Hopfield, J. Chem. Phys. 79 (1983) 2042.

12. T.J. Kang, W. Jarzęba, P.F. Barbara and T. Fonseca, Chem. Phys. 149 (1990) 81.

13. For recent reviews on the importance of solvation dynamics in electron transfer see: P.F. Barbara, G.C. Walker and T.P. Smith, Science 256 (1992) 975; M. Maroncelli, J. MacInnis and G.R. Fleming, Science 243 (1989) 1675.

14. A.M. Kjaer and J. Ulstrup, J. Am. Chem. Soc. 109 (1987) 1934.

15. F. Markel, N.S. Ferris, I.R. Gould and A.B. Myers, J. Am. Chem. Soc. 114 (1992) 6208.

16. I.R. Gould, R.H. Young, R.D. Moody and S. Farid, J. Phys. Chem. 95 (1991) 2068.

17. S. Ruhman, B. Kohler, A.G. Joly and K.A. Nelson, IEEE J. Quant. Electron. 24 (1988) 470.

18. J.C. Postlewaite, J.B. Miers, C.C. Reiner and D.D. Dlott, IEEE J. Quant. Electron. 24 (1988) 411.

19. D.A.V. Kliner, J.A. Alfano and P.F. Barbara, J. Chem. Phys., in press.

20. C. Reichardt, Angew Chem. Int. Ed. Eng. 18 (1979) 98.

21. For recent reviews on solvation dynamics see: P.F. Barbara and W. Jarzęba, Adv. Photochem. 15 (1990) 1; M. Maroncelli, J. Mol. Liq., in press.

22. N. Liang, J.R. Miller and G.L. Closs, J. Am. Chem. Soc. 112 (1990) 5353.

23. N.S. Hush, Prog. Inorg. Chem. 8 (1967) 391.

24. M. Maroncelli and G.R. Fleming, J. Chem. Phys. 89 (1988) 5044.

25. T. Fonseca and B. Ladanyi, J. Phys. Chem. 95 (1991) 2116.

26. S.J. Rosenthal, X. Xie, M. Du and G.R. Fleming, J. Chem. Phys. 95 (1991) 4715.

Table 1. Summary of Previously Reported 790nm Data for Betaine–30.

Solvent	τ (ps)	λ_{max}(nm)	τ_s (ps)
Acetonitrile	0.5	630	0.5
Acetone	0.7	687	0.8
Methyl Acetate	1.3	725	1.7
Ethyl Acetate	1.5	761	2.6
Benzene	2.7	840	–
Toluene	3.2	855	–
GTA	3.4	697	125
Benzonitrile	3.6	690	4.8

Table 2. Bleach Recovery Times (Electron Transfer Times) Measured Near the Absorption Maximum.

Solvent	τ (ps)	λ_{max} (nm)	λ_{probe} (nm)	Shift (cm^{-1})
Acetone	1.3	687	700	–270
2–Propanol	2.2	591	600	–254
Toluene	3.1	855	820	500
Benzonitrile	4.4	690	700	–207
GTA.	7	697	700	–61

Table 3. Best Fit Parameters for Betaine–30 in Alcohols with λ_{pump}=550 nm and λ_{probe}=550nm, 600nm. The shorter lifetime is indicative of the electron transfer time and the longer lifetime is indicative of the solvent cooling time.

Solvent	λ_{probe}	τ_1 (ps)	τ_2 (ps)	λ_{max} (nm)
MeOH	550	2.3	30	515
	600	1.0	20	
EtOH	550	3.8	20	551
	600	4.8	52	
1–PrOH	550	7	30	564
	600	2.3	90	
1–BuOH	550	6.5	50	570
	600	4.3	146	

Table 4. Experimental Dependence of Electron Transfer Time on Excitation Wavelength (λ_{probe}=700nm, which is close the the absorption maximum for acetone and GTA).

Solvent	λ_{pump}=800nm	λ_{pump}=700nm
Acetone	1.3 ± 0.3 ps	1.3 ± 0.1 ps
GTA	7.8 ± 2.4 ps	7.2 ± 0.4 ps

Table 5. Best Fit Parameters of Betaine–30 Absorption Spectra and Parameters used in Electron Transfer Simulations.

Solvent	V_{el}	ΔG°	λ_{QM}	ν_{QM}	$\lambda_{cl,vib}$	$\lambda_{cl,sol}$	τ_s
	<——— cm^{-1} ———>						ps
Acetone	1400	–10954	924	1736	1223	1881	0.83
GTA	1400	–10660	1372	1800	1223	1741	125

Table 6. Absorption Recovery Times at Nearly Constant Energy Shift.

Solvent	λ_{probe} (nm)	λ_{max} (nm)	Shift (cm^{-1})	τ (ps)
Acetone	790	687	1900	2.3
Benzonitrile	790	690	1830	4.7
Toluene	1000	855	1700	6.6
GTA	790	697	1690	>100
1–Butanol	640	570	1920	140

Table 7. The effect of an inertial component on the electron transfer rate.

Solvent	%Inertial	λ_{fast}	λ_{slow}	τ_a	τ_b
		<—— cm^{-1}	——>	<—— ps	——>
Acetone	0	0	1881	2.1	1.4
	20	376	1505	1.8	1.2
	40	752	1129	1.5	1.1
	60	1129	752	1.2	1.0
	80	1505	376	1.3	2.6
GTA	0	0	1741	7.4	9.1
	20	348	1393	3.5	5.0
	40	696	1045	1.5	2.2
	60	1045	696	0.6	0.8

Figure Captions

Fig. 1. The laser system. A modelocked Nd:YAG laser is used to synchronously pump a dye laser and seed a Nd:YAG regenerative amplifier. The dye laser output is amplified by the output of the regenerative amplifier. BS: beam splitter; AOM: acoustooptic modulator; SPS: single pulse selector; 2X: KTP frequency doubling assembly.

Fig. 2. An 800nm pump, continuum probe experimental setup. Continuum is generated in a 10mm cell containing H_2O and reamplified in an appropriate laser dye. BS: beam splitter; CG: continuum generation cell; IF: interference filter; CA: continuum amplification cell; C: chopper; S: sample cell; PD: photodiode.

Fig. 3. Transient pump–probe spectra of betaine–30 in acetone with $\lambda_{pump} = 800$ nm and $\lambda_{probe}=$ a) 800 nm, b) 700 nm, c) 640 nm, and d) 600 nm.

Fig. 4. Transient pump–probe spectra of betaine–30 in GTA with $\lambda_{pump} = 800$ nm and $\lambda_{probe} =$ a) 800 nm, b) 700 nm, c) 640 nm, and d) 600 nm.

Fig. 5. Transient pump–probe spectra of betaine–30 in toluene with $\lambda_{pump} = 780$ nm and $\lambda_{probe} =$ a) 1000 nm, b) 820 nm, c) 680 nm, and d) 580 nm.

Fig. 6. Transient pump–probe spectra of betaine–30 in 1–propanol with $\lambda_{\text{pump}} = 550$ nm and λ_{probe} = a) 790 nm, b) 720 nm, c) 600 nm, and d) 550 nm.

Fig. 7. Transient pump–probe spectra of betaine–30 in acetone with λ_{probe} 800 nm and λ_{pump} = a) 400 nm and b) 800 nm.

Fig. 8. Transient pump–probe spectra of betaine–30 in GTA with λ_{probe} 800 nm and λ_{pump} = a) 400 nm and b) 800 nm.

Fig. 9. Population dynamics in acetone assuming broadband excitation. a) shows the free energy curves for the reaction. b) shows the excited state population dynamics. c) shows the ground state population dynamics. In this picture, the residual ground state population has been subtracted for clarity.

Fig. 10. Population dynamics in GTA assuming broadband excitation. a) shows the excited state population dynamics. b) shows the ground state population dynamics. In this picture, the residual ground state population has been subtracted for clarity.

Fig. 11. Spectral dynamics in acetone assuming broadband excitation. a) Dynamics of the stimulated emission band due to the excited state population dynamics shown in Figure 9b. b) Dynamics of the bleach band due to the ground state dynamics shown in Figure 9c. c) The total transient spectrum.

Fig. 12. Spectral dynamics in GTA assuming broadband excitation. a) Dynamics of the stimulated emission band due to the excited state population dynamics shown in Figure 10a. b) Dynamics of the bleach band due to the ground state dynamics shown in Figure 10b. c) The total transient spectrum.

Fig. 13. Population dynamics in acetone assuming selective excitation at 700nm. a) shows the excited state dynamics. b) shows the ground state dynamics. In this picture, the residual ground state population has not been subtracted in order to emphasize the hole burning features.

Fig. 14. Spectral dynamics in acetone assuming selective excitation at 700nm.

Fig. 15. The survival probability, S(t), for acetone assuming different excitation conditions. Solid line: broadband; dashed line: 800nm; dotted line: 700nm; dashed–dotted line: 640nm.

Fig. 16. The survival probability, S(t) for GTA assuming different excitation conditions. Solid line: broadband; dashed line: 800nm; dotted line: 700nm; dashed–dotted line: 640nm.

Fig. 17. A comparison of the predicted and observed dynamics in GTA. a) 800nm probe. b) 700nm probe. c) 640nm probe.

Fig. 18. A comparison of the predicted and observed dynamics in acetone. a) 800nm probe. b) 700nm probe. c) 640nm probe.

Fig. 19. The effect of an inertial component on the spectral dynamics of acetone. a) %Inertial = 20%. b) %Inertial = 40%. c) %Inertial = 60%. d) %Inertial = 80%.

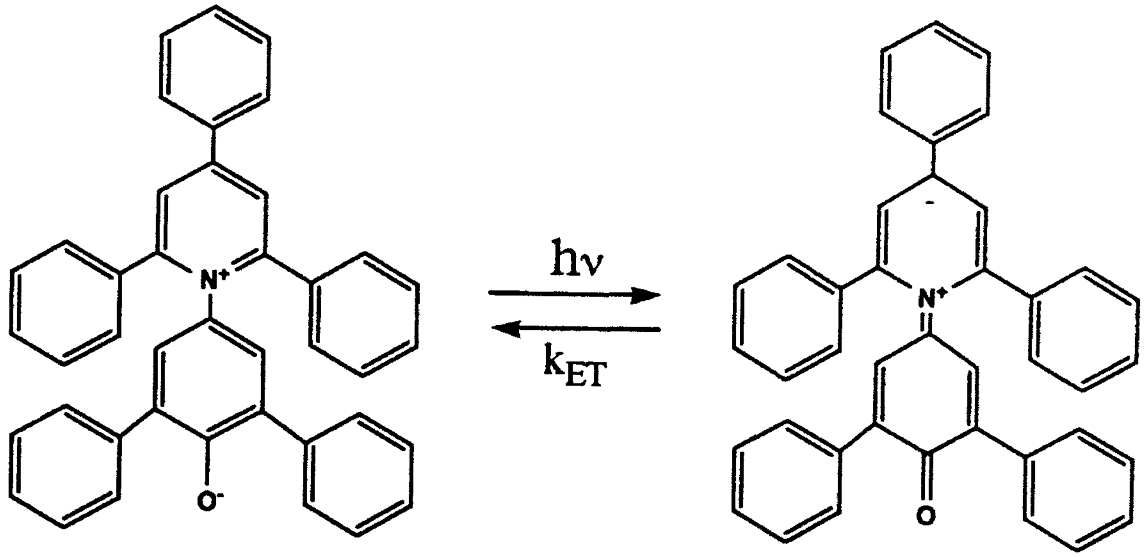

Scheme 1

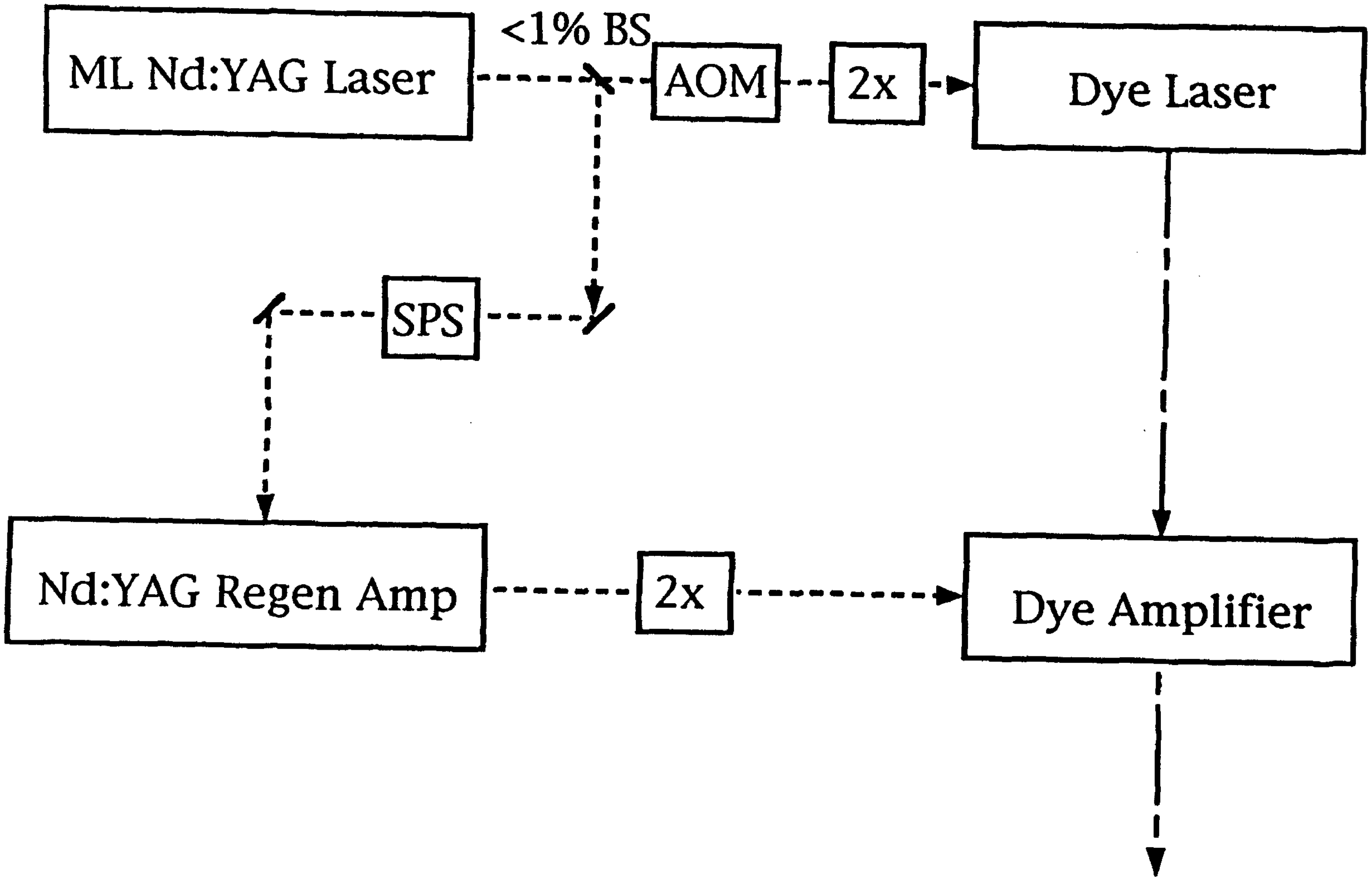
ML Nd:YAG Laser
<1% BS
AOM
2x
Dye Laser
SPS
Nd:YAG Regen Amp
2x
Dye Amplifier

Figure1

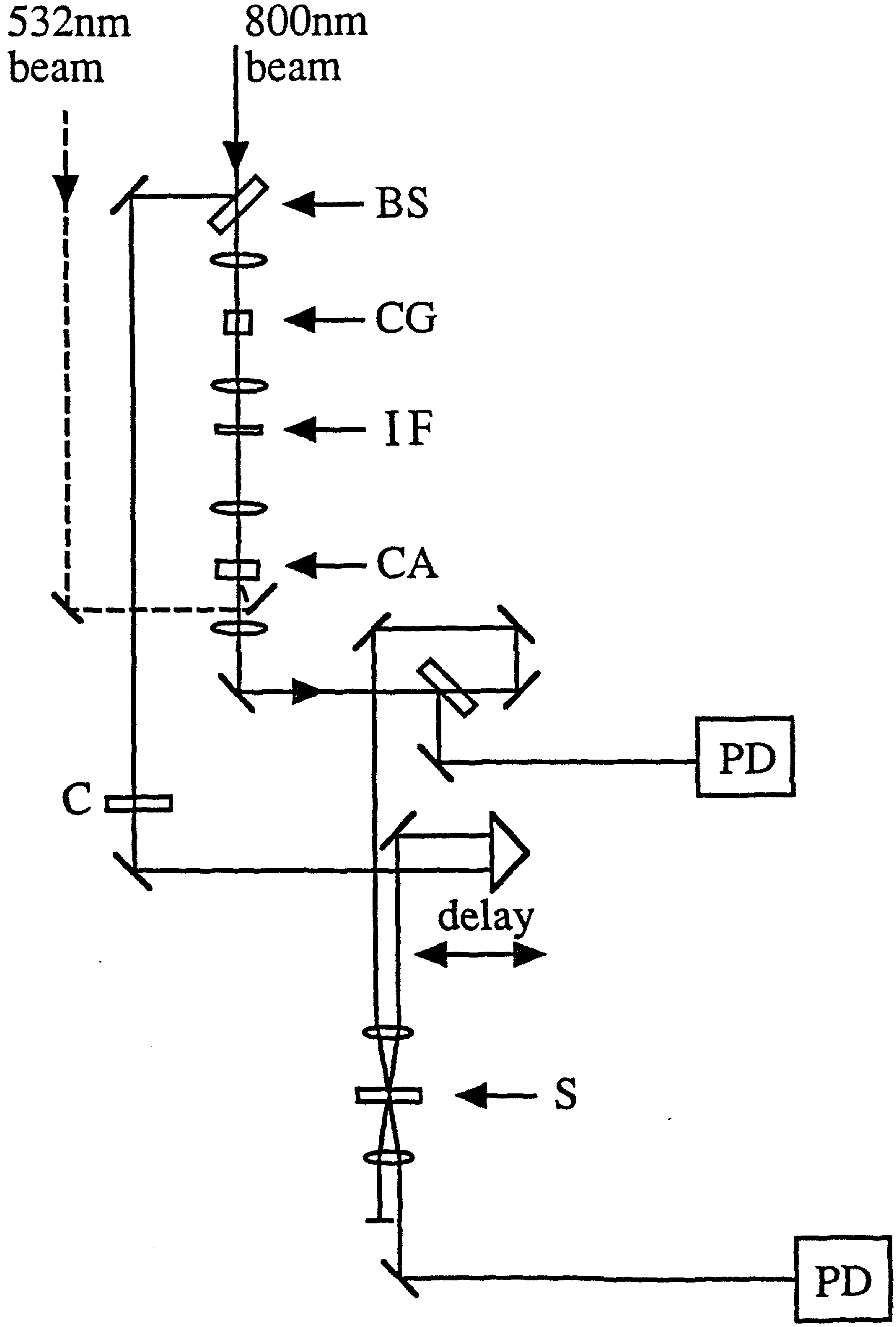

Figure 2

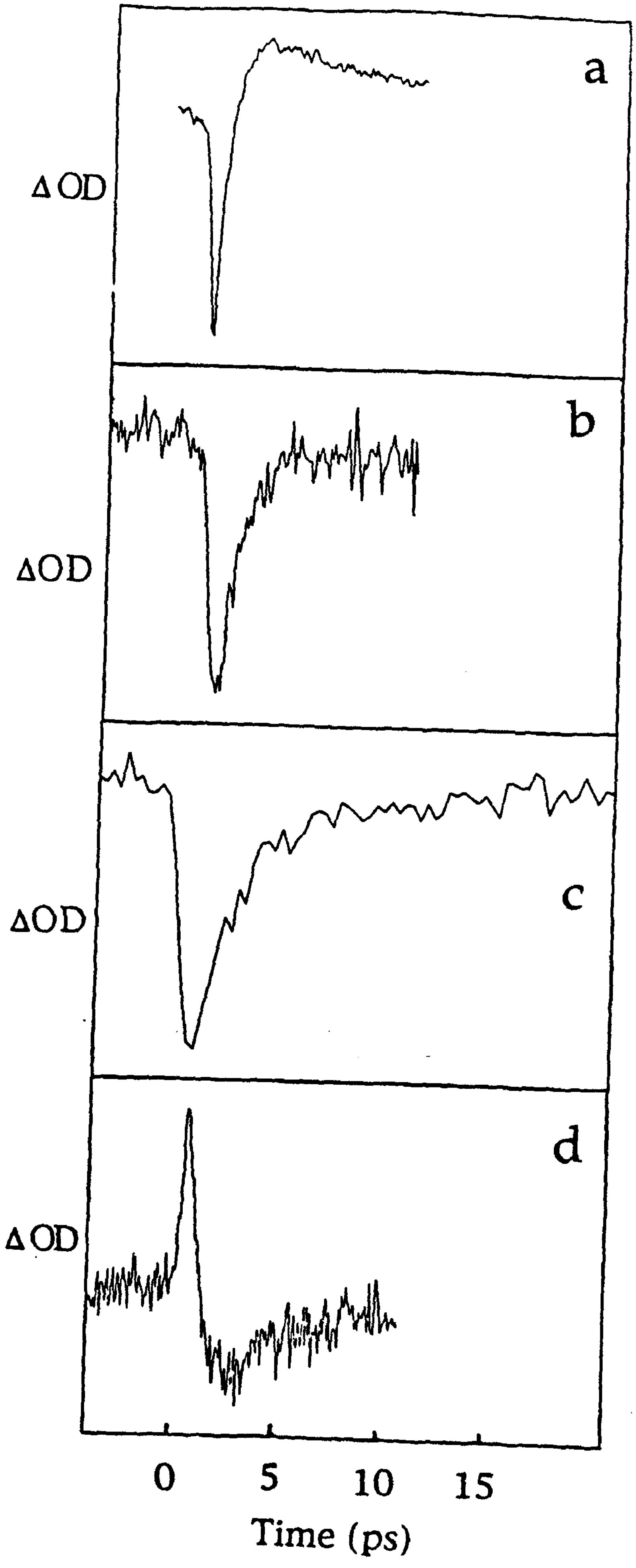

Figure 3

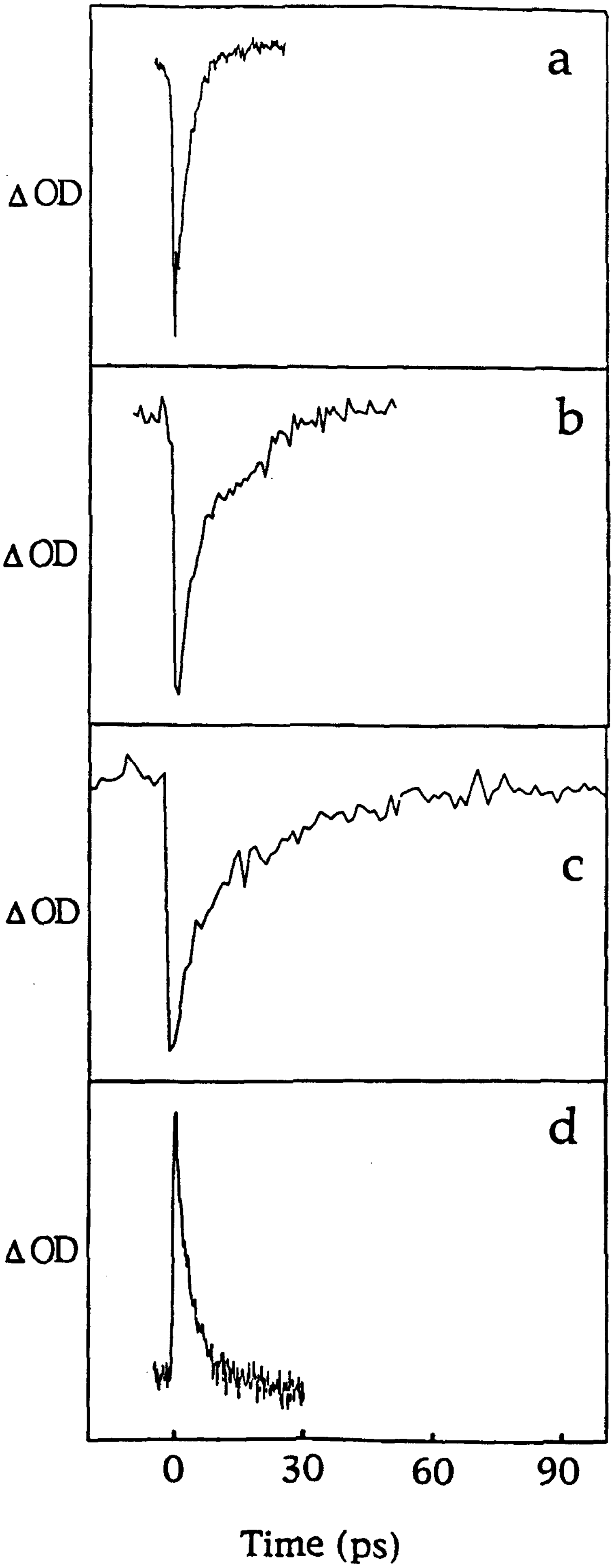

Figure 4

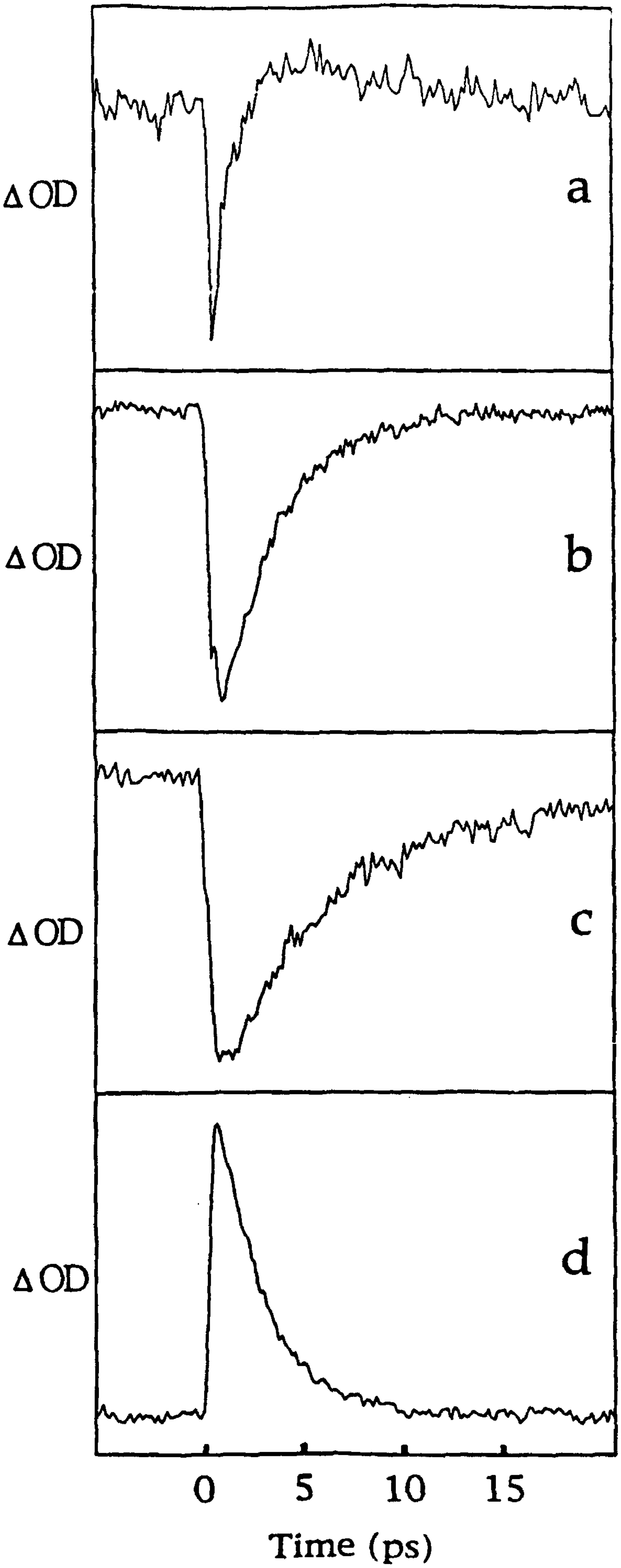

Figure 5

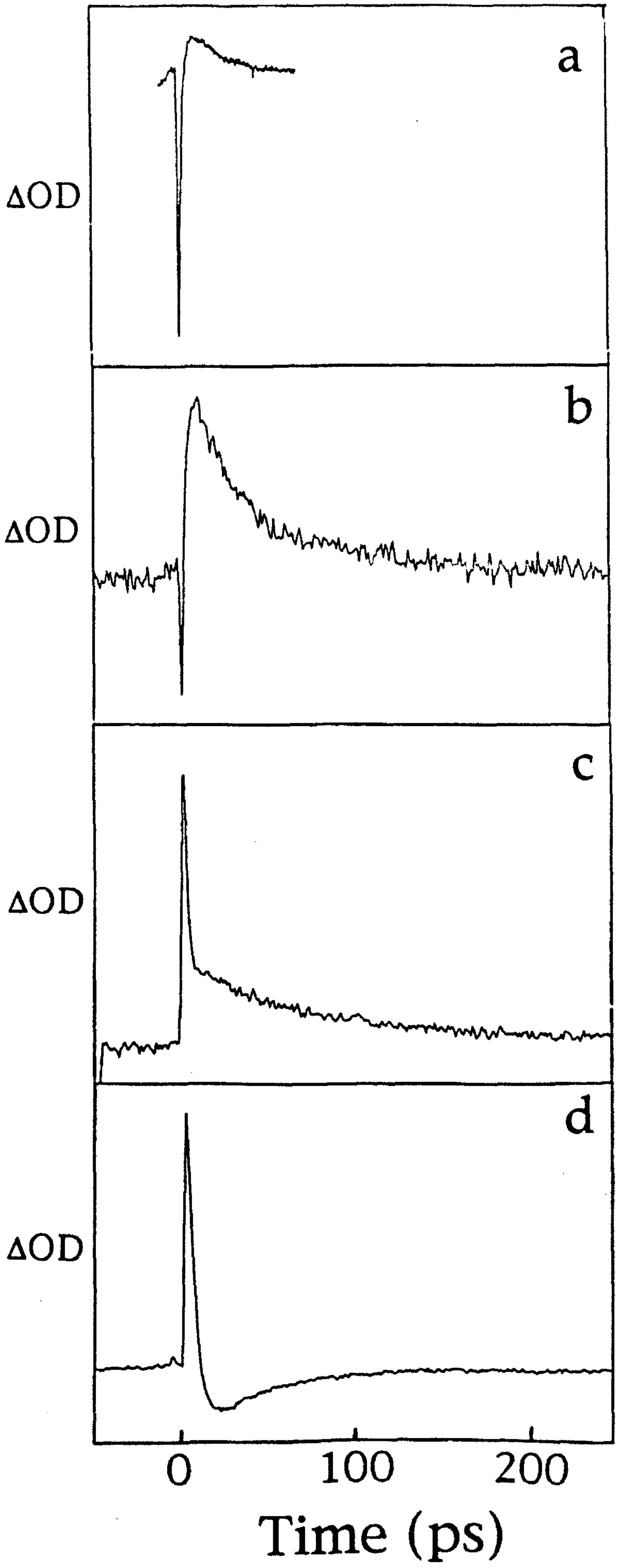

Figure 6

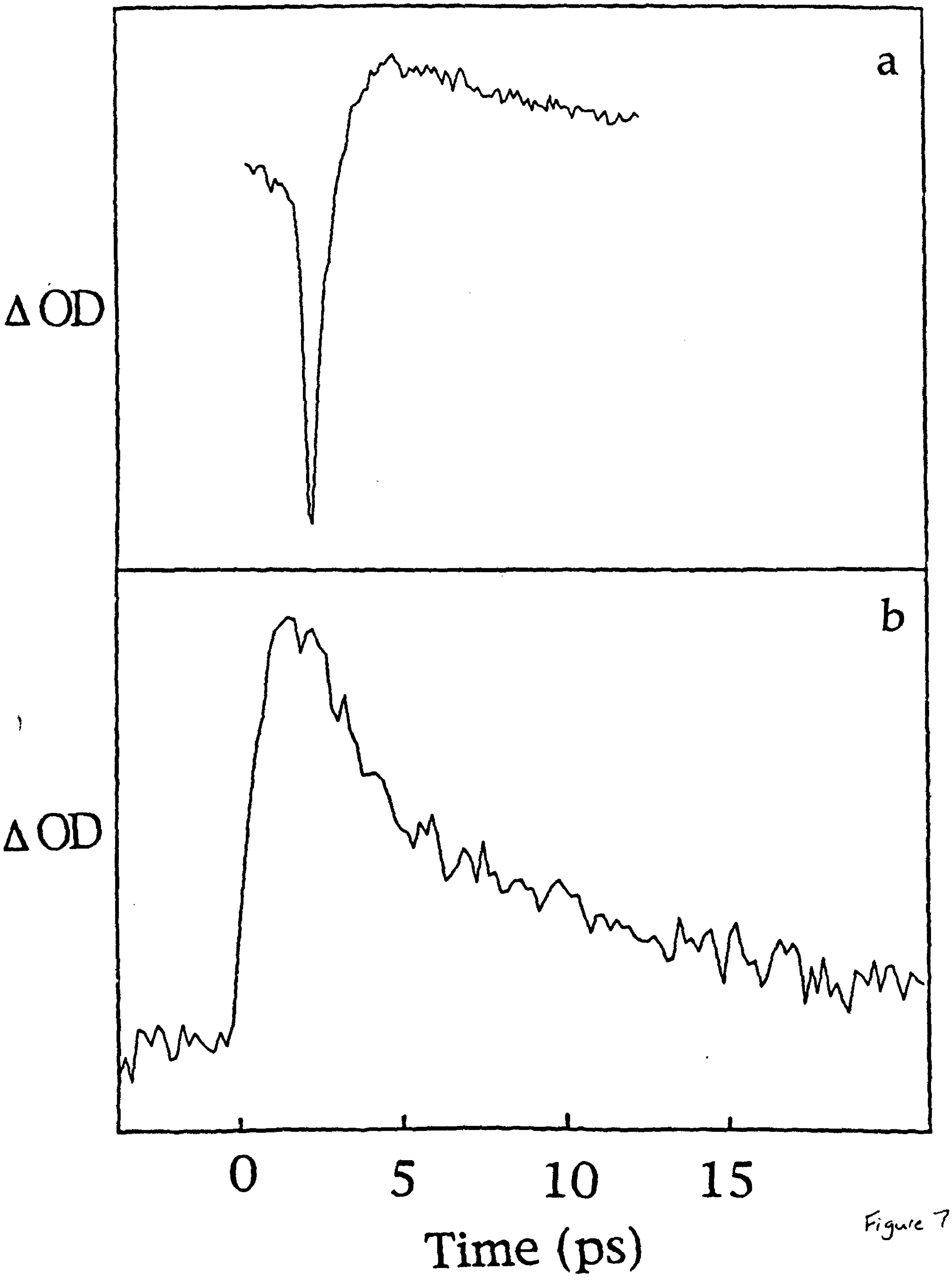

Figure 7

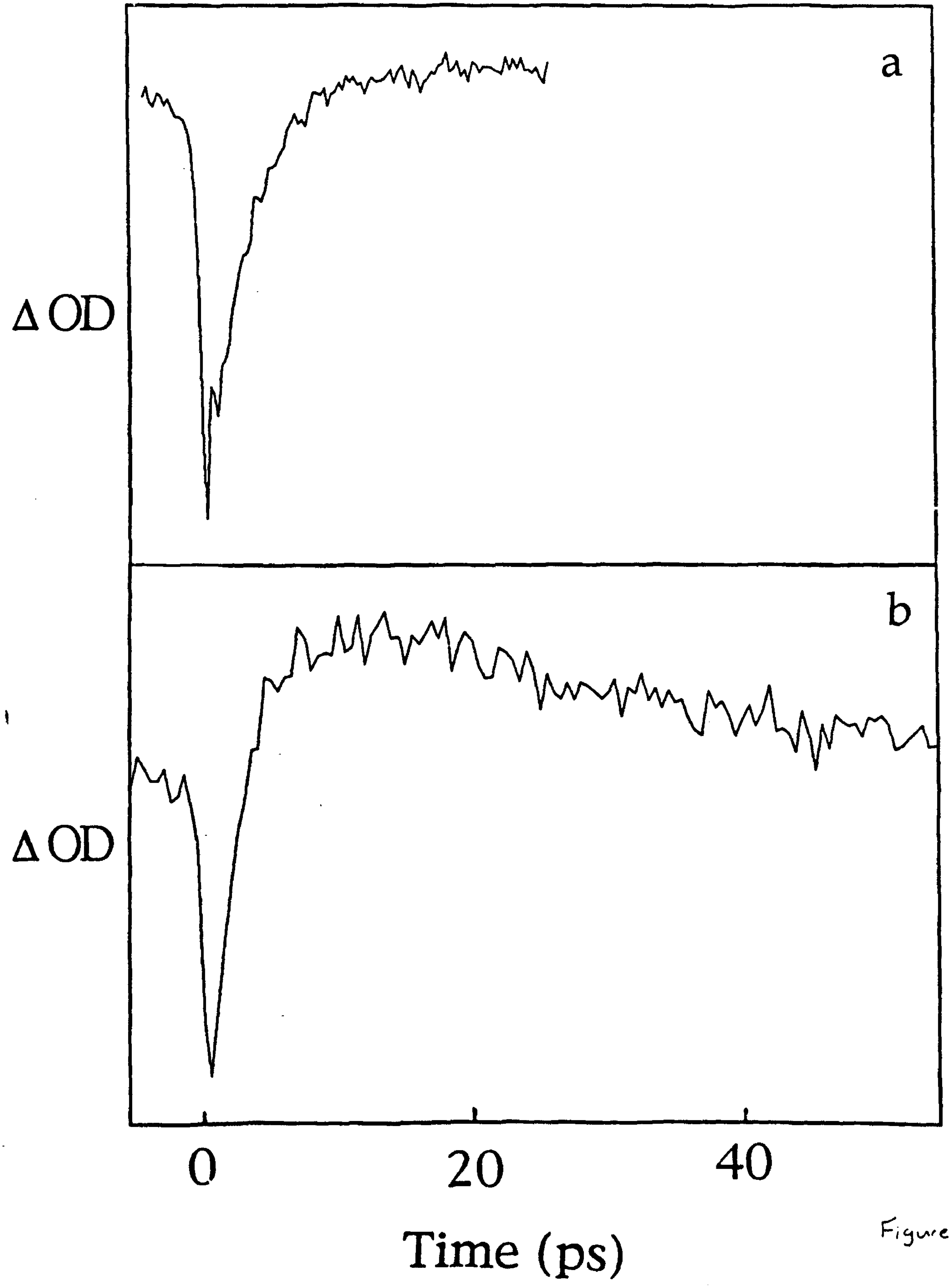

Figure 8

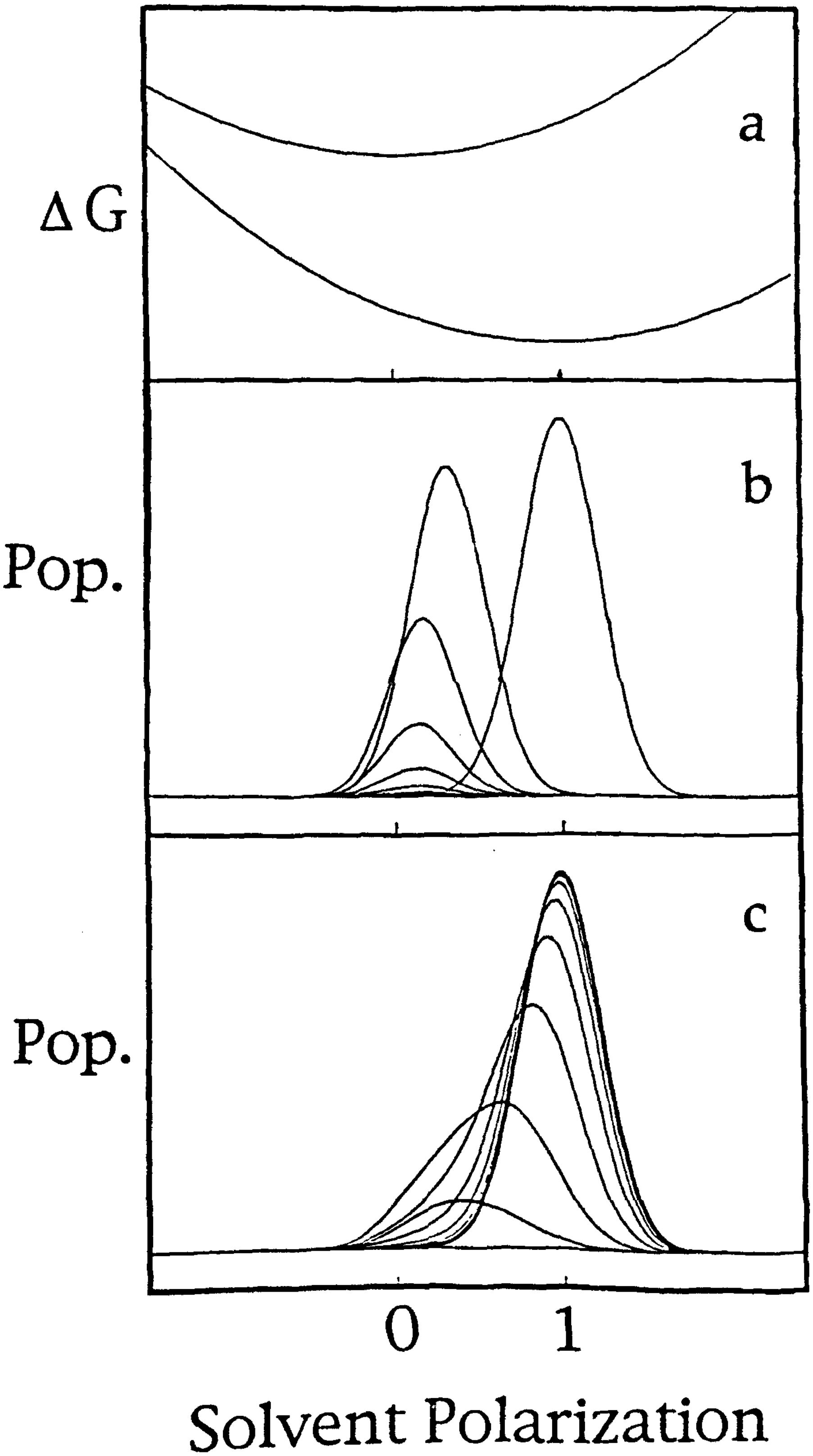

Figure 9

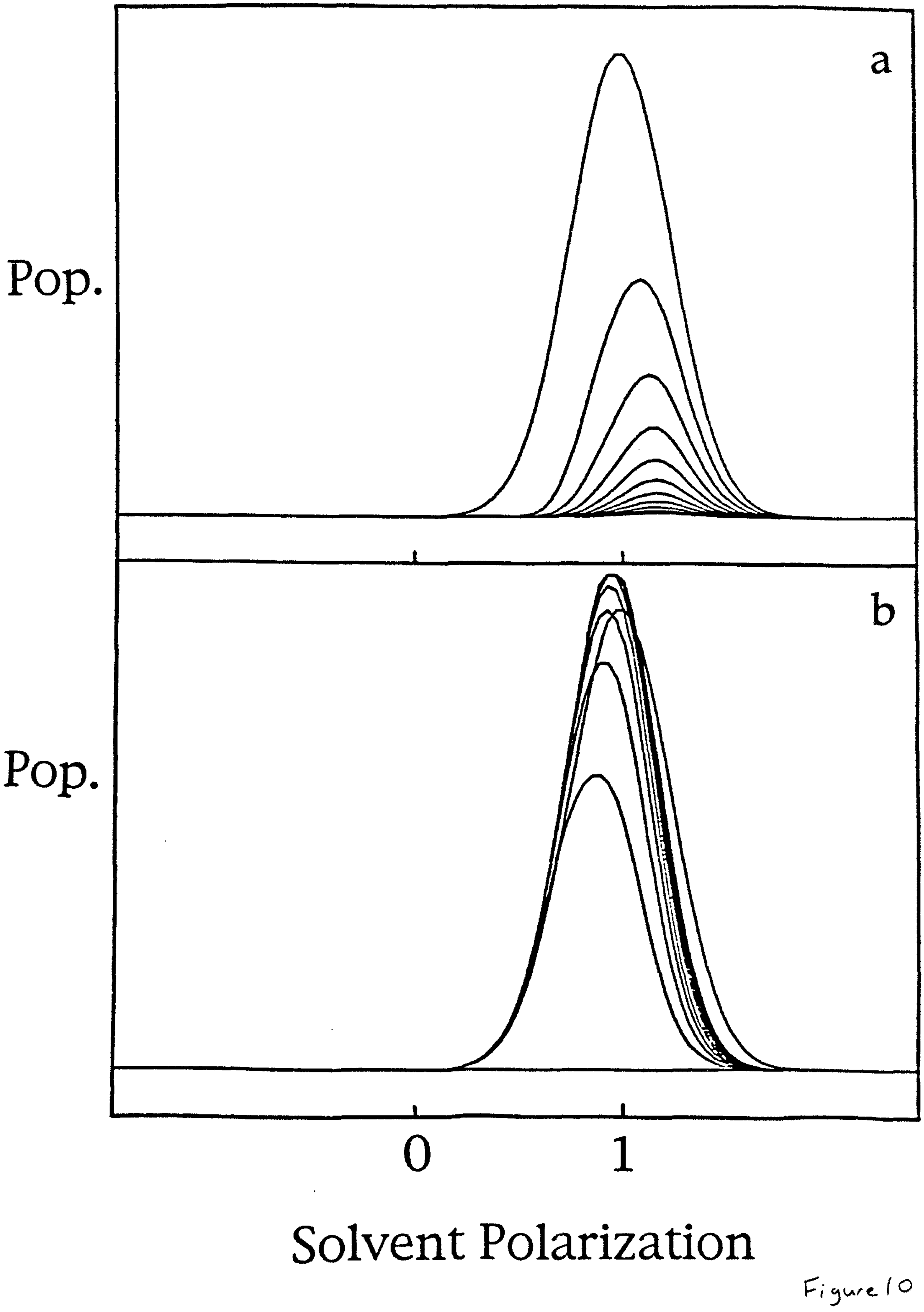

Figure 10

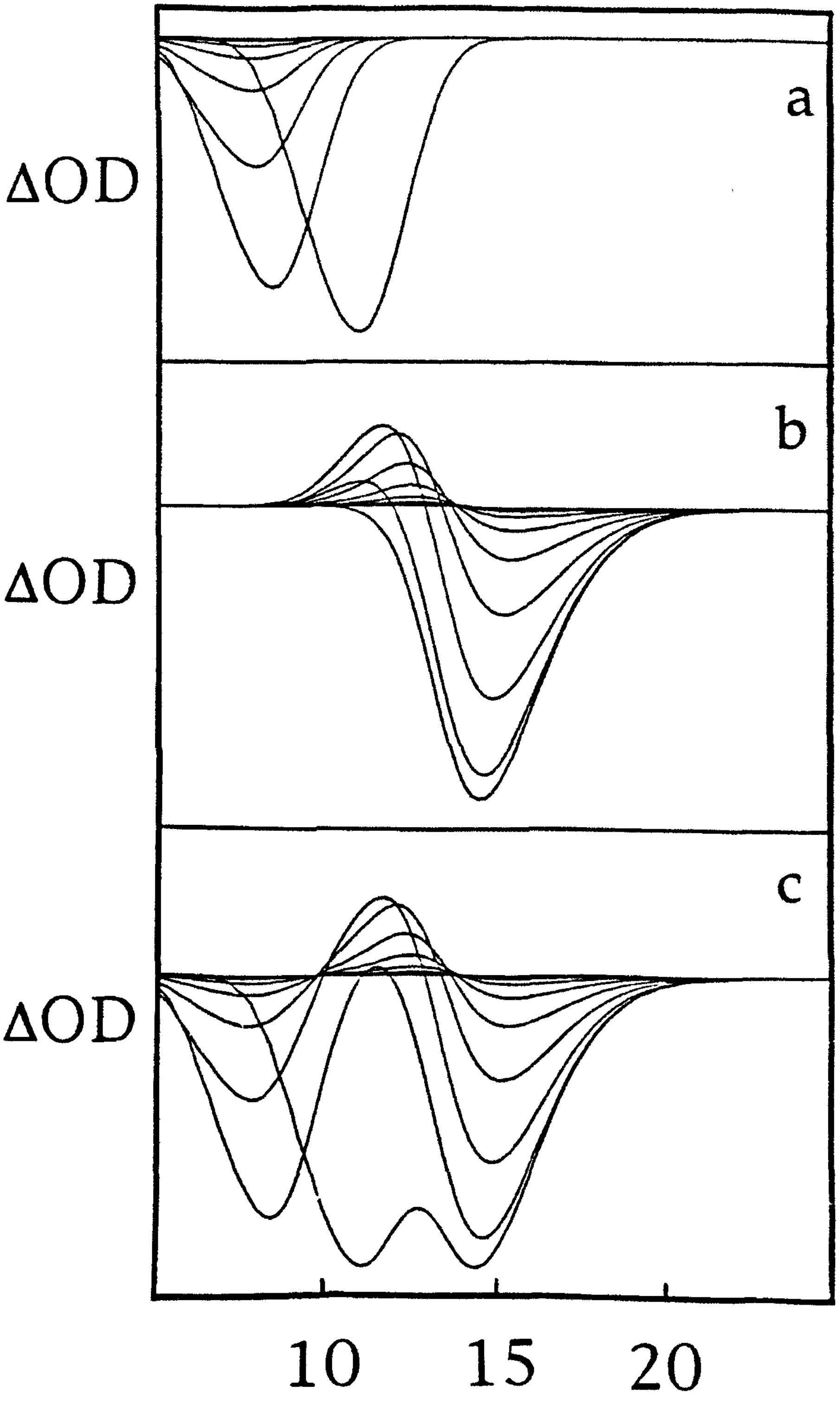

Figure 11

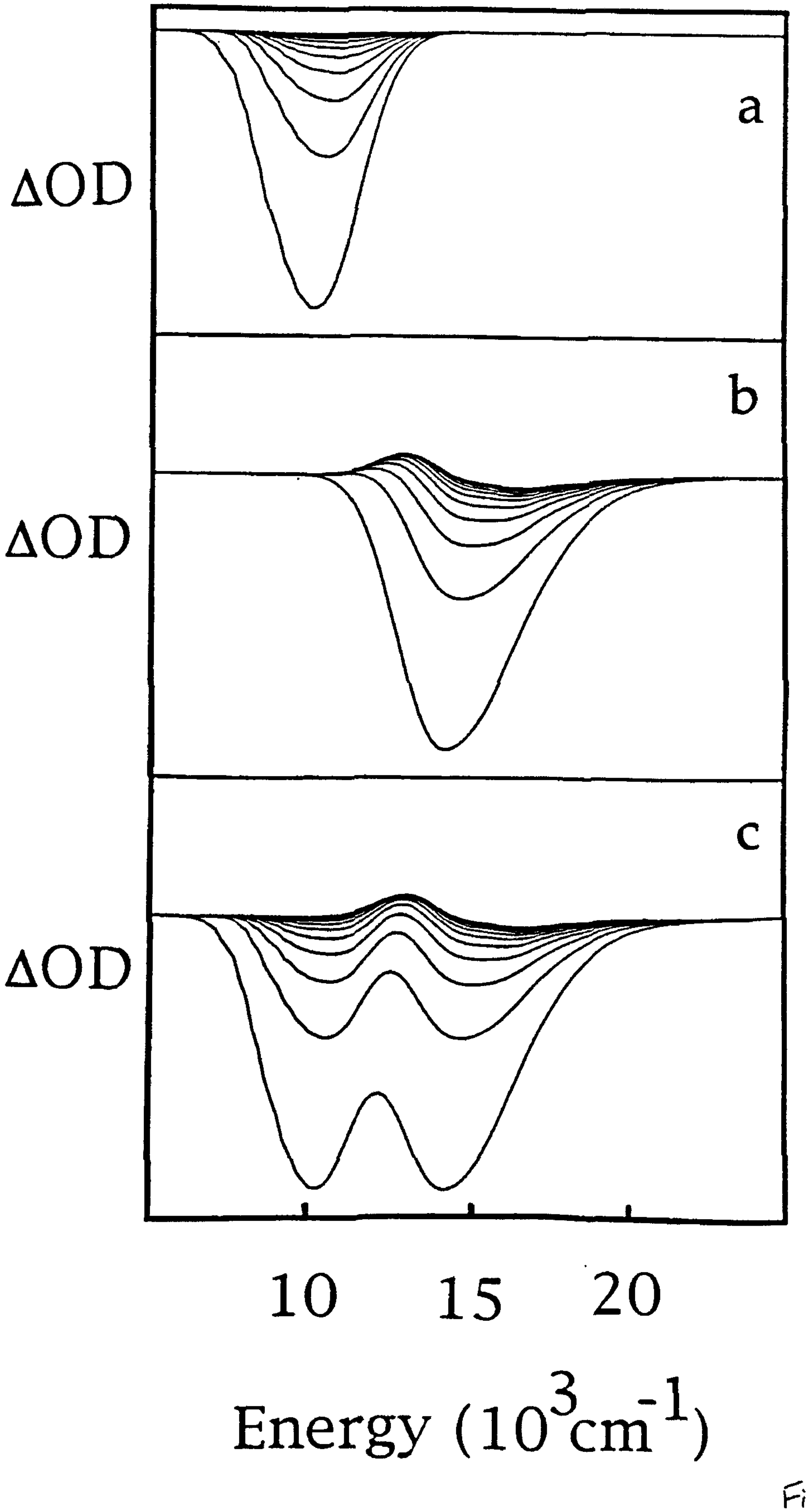

Figure 12

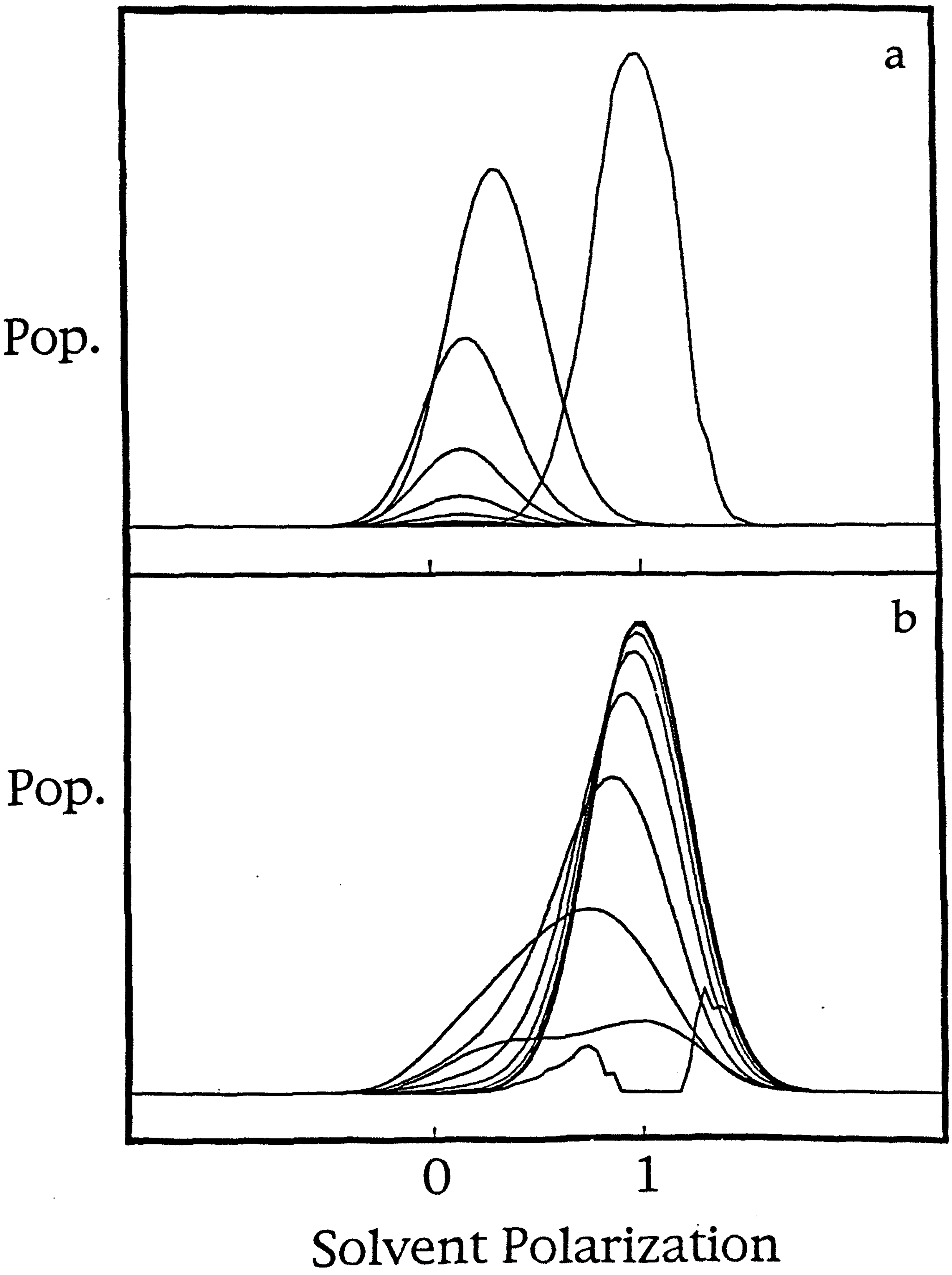

Figure 13

Figure 14

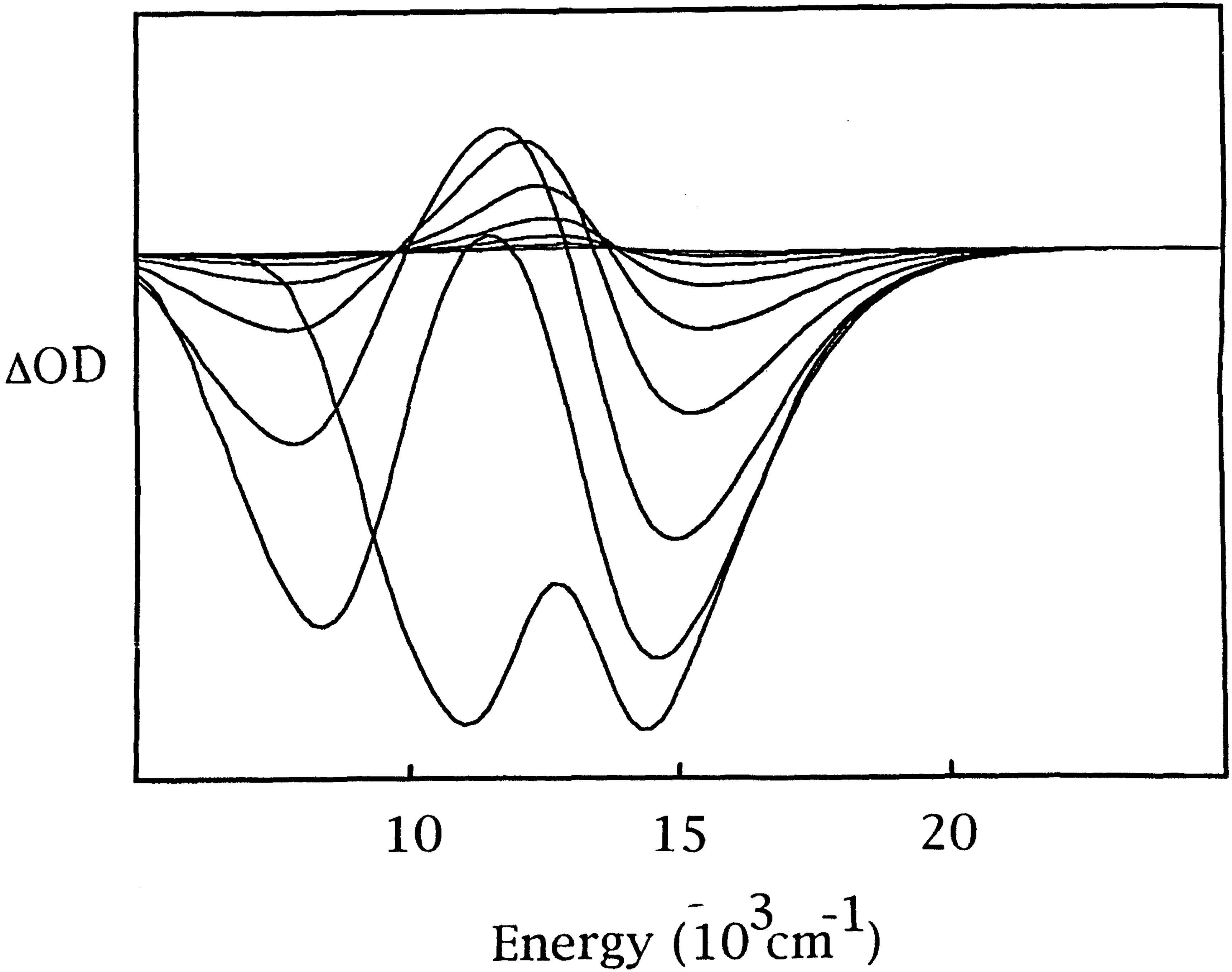

Figure 15

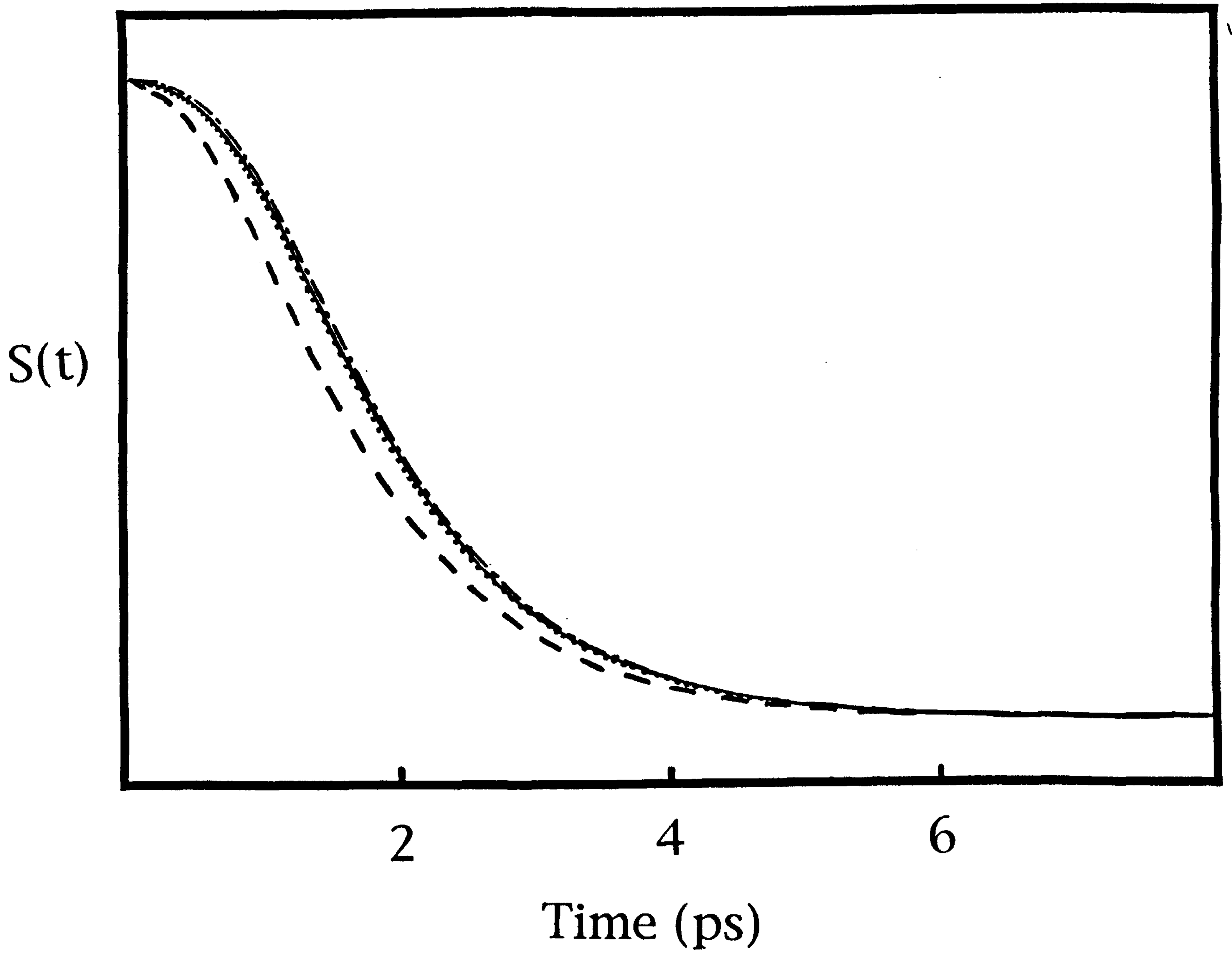

Figure 16

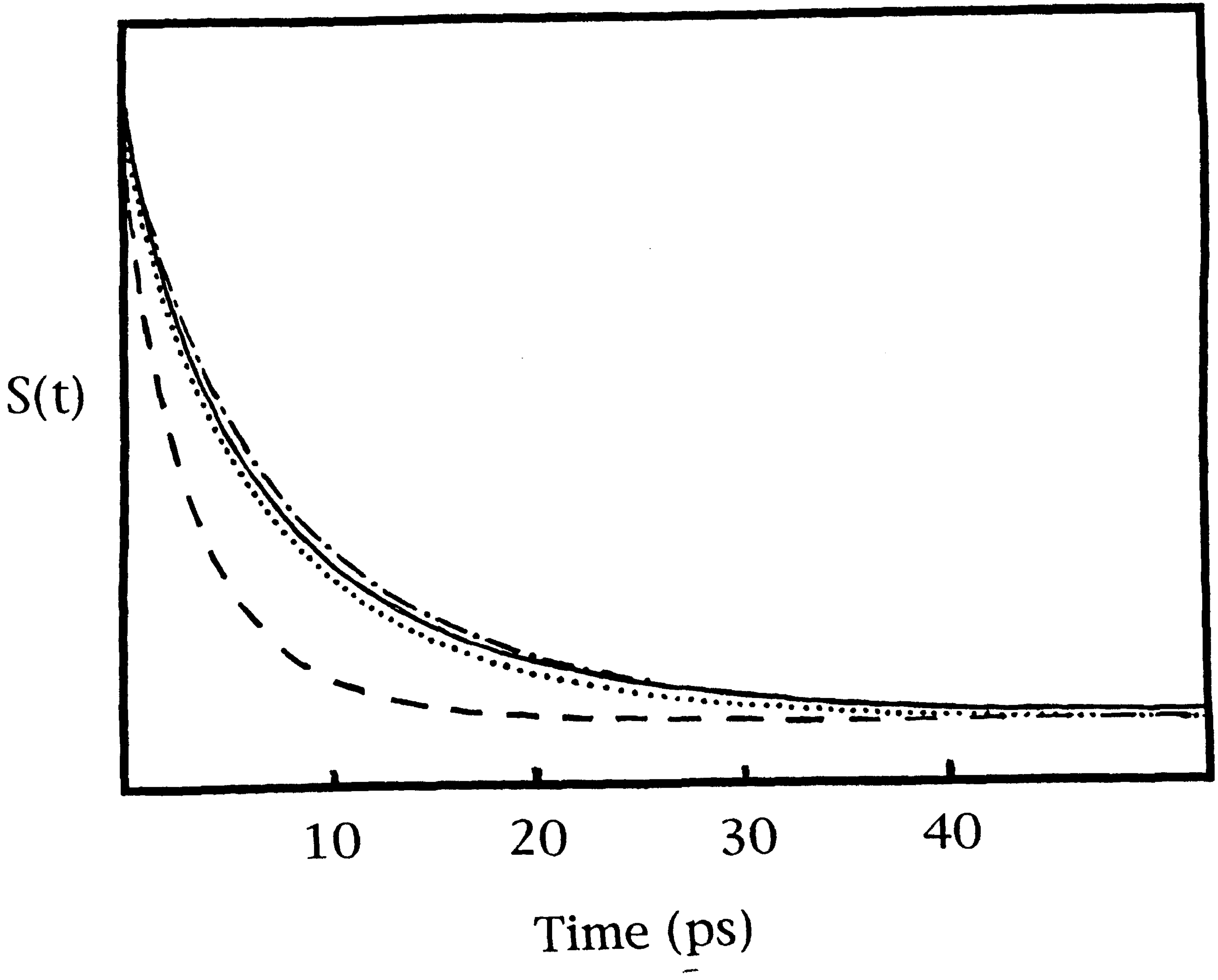

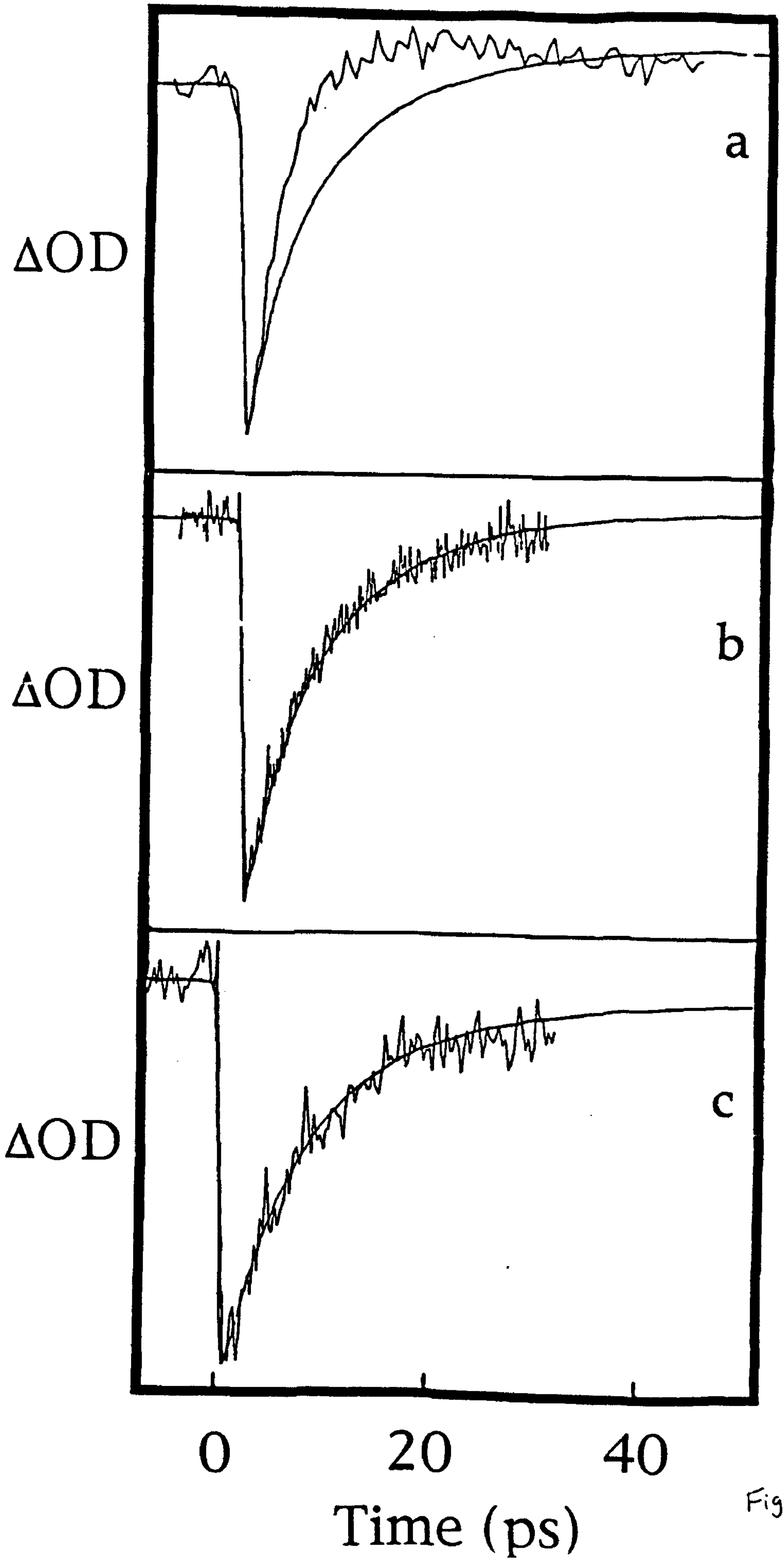

Figure 17

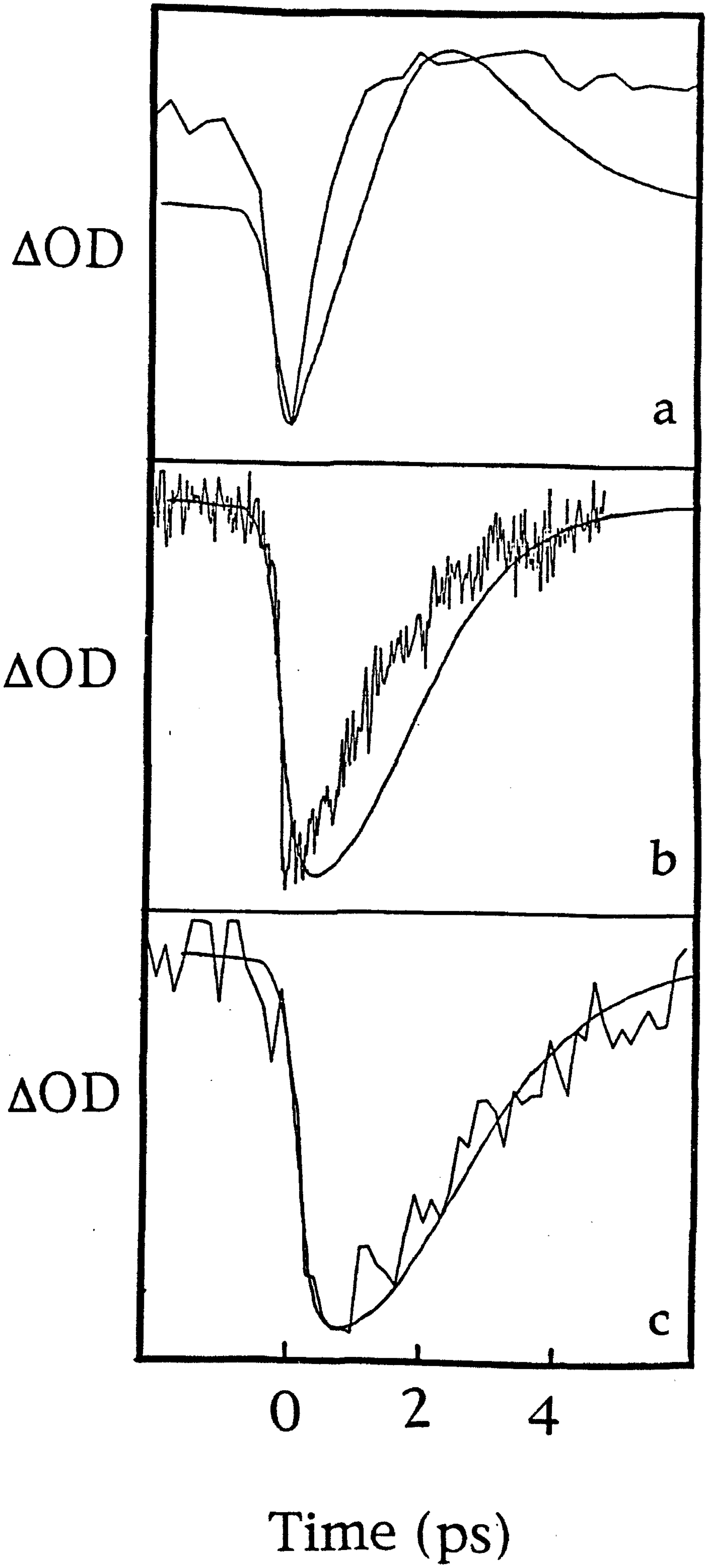

Figure 18

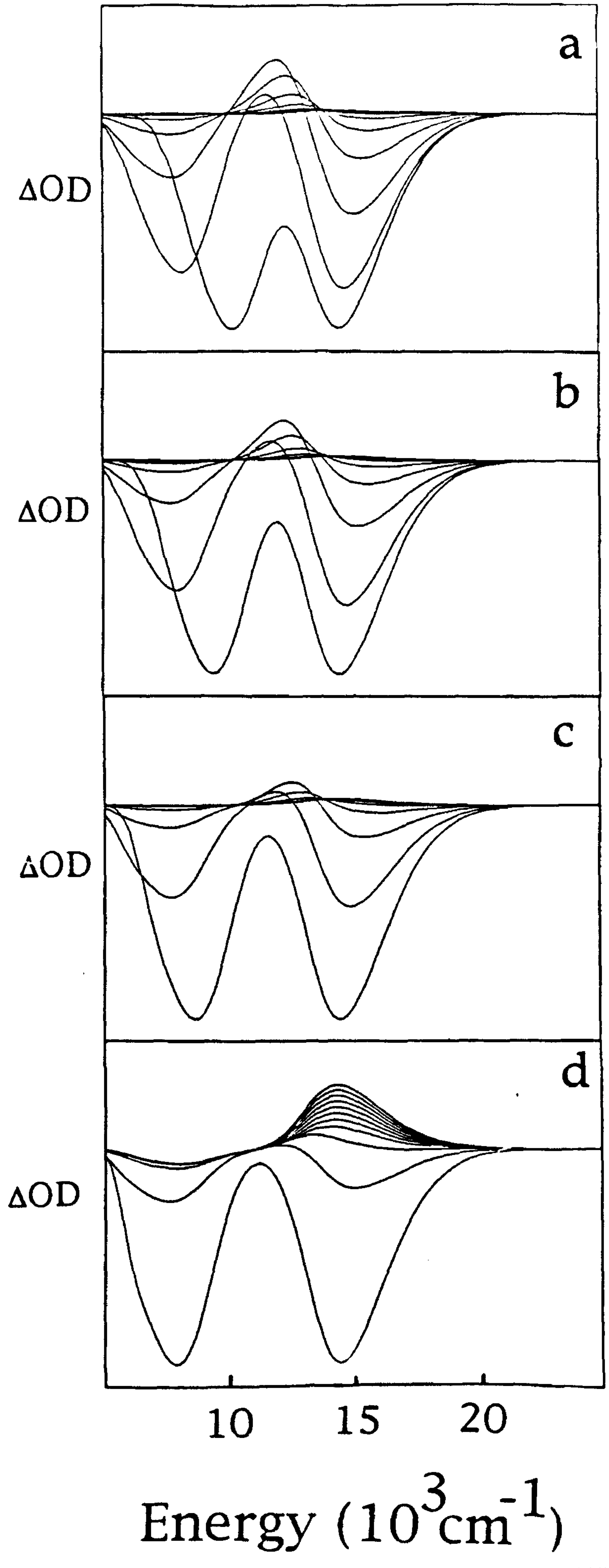

Figure 19